

# Satellite orbital drag during magnetic storms

D. M. Oliveira<sup>1,2</sup>, E. Zesta<sup>2</sup>

<sup>1</sup>Goddard Planetary Heliophysics Institute, University of Maryland, Baltimore County, Baltimore, MD  
USA

<sup>2</sup>Geospace Physics Laboratory, NASA Goddard Space Flight Center, Greenbelt, MD USA

## Key Points:

- Comprehensive spatiotemporal study of satellite orbital drag effects during magnetic storms caused by coronal mass ejections
- Stronger drag effects during early main phase of extreme storms occur at low latitudes due to Joule heating propagation from high latitudes
- Densities during the strongest storms show large uncertainties that continue throughout the recovery phase

Manuscript published in *Space Weather* (2019), 17, <https://doi.org/10.1029/2019SW002287>

arXiv:1910.09622v1 [physics.space-ph] 21 Oct 2019

---

Corresponding author: Denny Oliveira, [denny.m.deoliveira@nasa.gov](mailto:denny.m.deoliveira@nasa.gov)

## Abstract

We investigate satellite orbital drag effects at low-Earth orbit (LEO) associated with thermosphere heating during magnetic storms caused by coronal mass ejections. Challenge Mini-satellite Payload (CHAMP) and Gravity Recovery And Climate Experiment (GRACE) neutral density data are used to compute orbital drag. Storm-to-quiet density comparisons are performed with background densities obtained by the Jacchia-Bowman 2008 (JB2008) empirical model. Our storms are grouped in different categories regarding their intensities as indicated by minimum values of the SYM-H index. We then perform superposed epoch analyses with storm main phase onset as zero epoch time. In general, we find that orbital drag effects are larger for CHAMP (lower altitudes) in comparison to GRACE (higher altitudes). Results show that storm-time drag effects manifest first at high latitudes, but for extreme storms particularly observed by GRACE stronger orbital drag effects occur during early main phase at low/equatorial latitudes, probably due to heating propagation from high latitudes. We find that storm-time orbital decay along the satellites' path generally increases with storm intensity, being stronger and faster for the most extreme events. For these events, orbital drag effects decrease faster probably due to elevated cooling effects caused by nitric oxide, which introduce modeled density uncertainties during storm recovery phase. Errors associated with total orbit decay introduced by JB2008 are generally the largest for the strongest storms, and increase during storm times, particular during recovery phases. We discuss the implication of these uncertainties for the prediction of collision between space objects at LEO during magnetic storms.

## Plain Language Summary

In this work, we investigate the effects caused by atmospheric drag forces on satellites orbiting Earth in the upper atmosphere (~300-500 km altitude) during magnetic storms caused by solar perturbations. Atmospheric drag forces during storms have been recognized by the Federal Government as a natural hazard that could severely impact satellites and human assets that fly in the upper atmosphere by affecting their continuous tracking and re-entry processes, as well as significantly reducing their lifetimes. Examples are communications satellites and the International Space Station. We use atmospheric density data, a very important ingredient for orbital drag calculations, to investigate spatiotemporal patterns of their response. By assessing the performance of an empirical model when predicting orbital drag effects, we find that the model introduces uncertainties in atmospheric density computations particularly during the recovery of the most extreme storms. We then suggest physical mechanisms that should be incorporated by the model in order to reduce errors associated with atmospheric densities.

## 1 Introduction

The Sun is a very active and the closest star to the Earth. Due to the high variability of the solar magnetic field, the Sun presents a solar cycle whose period is around 22 years, but the alternation between maximum and minimum sunspot numbers (SSNs) is approximately 11 years (Eddy, 1976). The Sun produces disturbances that propagate explosively away from it in the interplanetary space and eventually encounter Earth in their way. The most important disturbances with potential space weather impacts are the so called coronal mass ejections (CMEs). CMEs are more numerous when the Sun displays an active behavior linked to high SSN levels (Gosling et al., 1991; Ramesh, 2010). CMEs usually consist in three different parts: a leading edge with a shock, magnetic material or inner core, and a magnetic void (Illing & Hundhausen, 1985). Usually CMEs are the cause of intense-to-extreme magnetic storms as a result of the occurrence of magnetic reconnection between the interplanetary magnetic field (IMF) and the geomagnetic field when IMF is directed southward and lasts for at least a few hours (Gonzalez & Tsu-

rutani, 1987; Gonzalez et al., 1994). In general, the magnetic field structure that follows CME leading edges lead the high-latitude thermosphere to higher heating levels than CME-shock compressions (Lugaz et al., 2016; Kilpua et al., 2019).

The magnetosphere is strongly driven during magnetic storms. During active times, large amounts of energy and momentum are transported from the magnetosphere through field-aligned currents and injected into the high-latitude ionosphere-thermosphere system (Fuller-Rowell et al., 1994; Liu & Lühr, 2005; Prölss, 2011; Emmert, 2015; Lu et al., 2016; Kalafatoglu Eyiguler et al., 2018). This electromagnetic energy input increases the ion motion which in turn enhances the collision between ions and neutral particles in the ionosphere. As a result, neutral particles are heated and move towards higher regions in the upper atmosphere, or the thermosphere (Forbes, 2007; Prölss, 2011; Emmert, 2015). In addition, global wind surges characterized by large-scale gravity waves are generated at high latitudes and transport energy towards middle and low latitudes (Fuller-Rowell et al., 1994). Such waves are known as traveling atmospheric disturbances, or TADs (Richmond & Matsushita, 1975). TADs play an important role in causing global heating and energy distribution in the thermosphere (Hunsucker, 1982; Hocke & Schlegel, 1996; Bruinsma & Forbes, 2007). For instance, Sutton et al. (2009) showed that a series of CME-driven magnetic storms was the cause of thermosphere heating 2 hours at high latitudes and 3.5-4.0 hours at equatorial latitudes after the CME impacts. Such energy propagation was associated with TADs. Oliveira et al. (2017) showed with a superposed epoch analysis (SEA) study of thermosphere heating due to magnetic storms caused by CMEs that energy and heating propagate via TADs from high latitudes to equatorial latitudes within the average time of 3 hours after storm main phase onset. As a result, LEO satellites that happen to fly in those regions find themselves in regions with enhanced neutral mass density levels and experience increased effects related to atmospheric air drag forces (Chopra, 1961; King-Hele, 1987; Moe & Moe, 2005; Prölss, 2011; Prieto et al., 2014; Emmert, 2015; Zesta & Huang, 2016).

Perhaps the first clear connection between enhanced satellite orbital drag effects and magnetic activity was reported very early in space age by Jacchia (1959). He studied ephemeris data from the Russian Sputnik 1958 $\delta$ 1 spacecraft and discovered that the satellite acceleration increased significantly during a magnetic active period. Current data show that the main phase of that storm of 8-9 July 1958 ended at Dst (disturbance storm time index, used to quantify magnetic storm intensities) values smaller than  $-300$  nT. The spacecraft decelerated because of its loss of gravitational potential energy and the consequent gain of kinetic energy, which led to a decrease in altitude (Prölss, 2011; Prieto et al., 2014; Emmert, 2015; Zesta & Huang, 2016). Jacchia (1959) correctly attributed this effect to the upwelling of neutral particles from the lower to the upper atmosphere. This pioneer observation sparked the interest of many scientists in the following decades in producing empirical models to estimate densities in the thermosphere (Jacchia, 1970; King-Hele, 1987; Mayr et al., 1990; Picone et al., 2002; Storz et al., 2002; Prölss, 2011; S. L. Bruinsma, 2015; Emmert, 2015; Yamazaki et al., 2015; Weng et al., 2017; S. Bruinsma et al., 2018; Mehta et al., 2018; Sutton, 2018). He et al. (2018) have provided a review on the comparison between empirical thermosphere neutral mass density models commonly used in the past decades.

The understanding and improvement of prediction capabilities of satellite orbital drag during storm times is of paramount importance in current space weather investigations and orbit-prediction data product conceptions. Correctly predicting and forecasting orbital drag can lead to satellite collision avoidance, reentry precision of decommissioned satellites, and increase of satellite life times (Prölss, 2011; Emmert, 2015; Zesta & Huang, 2016; He et al., 2018). For example, the U.S. Department of Defense's Space Surveillance Network is a program whose mission is to identify, catalogue, and track artificial space objects/debris orbiting Earth. This network keeps track of more than 2,000 objects larger than 10 cm that could potentially collide with active LEO satellites which

could in turn lead to their complete damage and losses. For instance, space debris produced by the event involving the total destruction of the Chinese meteorological satellite Fengyan 1C in 2007 immediately increased the collision risk of LEO satellites by approximately 10% (Pardini & Anselmo, 2009; Zesta & Huang, 2016). In addition, the unexpected collision between two communications satellites, the active American Iridium 33 satellite and the inactive Russian Cosmos 2251 satellite, increased the space debris by nearly 25% (Wang, 2010). The accuracy improvement of satellite orbital decay predictions during magnetic storms can play an important role as a tool in preventing the occurrence of the Kessler Syndrome, which was suggested by Kessler and Cour-Palais (1978). The authors predicted with simulations that successive collisions of LEO spacecraft with other spacecraft and/or space debris would increase the debris population exponentially and subsequently lead to a cascade of high collision levels triggered by the augmented debris levels in space. This would lead to the ultimate scenario of some forbidden orbit regions to LEO satellites due to high risk of collisions there. Satellite orbital drag has been identified by the U.S. Federal Government as a natural hazard that could “disrupt satellite, aircraft, and spacecraft operations; telecommunications; position, navigation, and timing services”, as identified by the National Space Weather Strategy. The subsequent National Space Weather Action Plan further outlines goals and roadmaps in order to successively protect human assets in space and on the ground from space weather threats. See a general introduction and links to these documents in Lanzerotti (2015) and Jonas and McCarron (2016).

Recently, Krauss et al. (2018) investigated the effects of magnetic storms on the subsequent drag forces on two LEO missions, CHAMP (CHALLENGE Mini-satellite Payload, Reigber et al., 2002) and GRACE (Gravity Recovery And Climate Experiment, Tapley et al., 2004). They found that satellite orbital decay rates and the subsequent time-integrated orbital decay show a strong dependence on the spacecraft’s altitude. The authors reported that the orbital decay at CHAMP altitudes were approximately three times larger than the total orbital decay at GRACE altitudes during the severe storm of 24 August 2005. These authors showed that mild storms can cause orbital decays at CHAMP altitudes whose magnitudes are comparable to orbital decays at GRACE altitudes caused by much more intense storms. In addition, Krauss et al. (2018) showed that the orbital decay of CHAMP and GRACE were strongly associated with minimum values of IMF  $B_z$  and SYM-H recorded during storm main phases, where the lower  $B_z$  and SYM-H, the more severe the orbital decay. In a previous work, Krauss et al. (2015) showed that the orbital decay associated with the GRACE spacecraft during the most extreme magnetic storm in the CHAMP/GRACE era (20 November 2003) was  $\sim 70$  m approximately 60 hours after that storm main phase onset.

Despite all these efforts, a statistical study that quantifies general statistical patterns of satellite orbital drag response to magnetic storms caused by CMEs, particularly with different storm intensity levels, still lacks in the literature. The main goal of this work is to fill in this gap. In addition, we will address the capability of an empirical thermosphere model of predicting satellite orbital decay effects during CME storms with different intensities. We will address the possible causes of uncertainties arising during storm times, which are of particular importance when computing probabilities and predictions for collisions of space objects during magnetically active times.

In this paper, we present for the first time an SEA study of the spatiotemporal LEO satellite orbital drag effects with 217 magnetic storms caused by CMEs in the period May 2001 to December 2015. Our particular interest is in the spatial and temporal patterns of orbital drag effects induced by heating propagation from auroral latitudes toward equatorial latitudes, as well as effects introduced by CHAMP and GRACE altitudes. The thermosphere neutral mass density data were obtained from accelerometers on-board the CHAMP and GRACE missions. The background or quiet density was computed with a thermosphere empirical model. Data and model will be presented in section 2, as well as the

techniques used for satellite orbital decay computations. The storm of 24 August 2005 will be used to illustrate our approach in section 3. Section 4 presents the main results. Finally, section 5 concludes the paper.

## 2 Data, model and orbital drag computations

### 2.1 Catalogue of coronal mass ejections

We use the CME catalogue provided and maintained by Dr. Ian Richardson and Dr. Hillary Cane (Richardson & Cane, 2010). Observation times in the solar wind at L1 upstream of the Earth of plasma and IMF data (next subsection), as well as shock-associated sudden impulse times and minimum Dst values are provided by the catalogue. Main information on techniques used to build and maintain this catalogue is outlined by Richardson and Cane (2010).

### 2.2 Interplanetary magnetic field, magnetic index, and sunspot number data

The IMF data are obtained from the OMNI database. IMF is represented in the geocentric solar magnetospheric system. The data are shifted to the magnetopause nose (at  $X = 17R_E$ ) and the techniques used to accomplish this were outlined by King and Papitashvili (2005). The IMF data has 1-min time resolution.

In this work, magnetic activity is indicated by the SYM-H index delivered by the World Data Center in Kyoto, Japan. The SYM-H index is similar to the well-known 1-hour resolution Dst index, but it has resolution of 1 minute. We use the former as opposed to the latter because we are interested in thermosphere changes within the time domain of minutes. The SYM-H index was first suggested by Iyemori (1990).

Solar activity is indicated by the monthly-averaged SSN data. The SSN data are compiled by SILSO (Sunspot Index and Long-term Solar Observations) of the Royal Observatory of Belgium, in Brussels. An entire *Solar Physics* issue has been dedicated to the recent recalibration methods used to determine SSNs (Clette & Lefèvre, 2016).

### 2.3 Neutral mass density data

We use data from two LEO satellites, namely CHAMP and GRACE. CHAMP was launched on 15 July 2000 and reentered on 19 September 2010. The mission started to orbit Earth at the initial altitude 456 km passing through Earth's poles in time intervals near 90 minutes with orbit inclination  $87.25^\circ$ . CHAMP precessed around Earth completing a full longitudinal cycle around the planet in approximately 131 days. The mission was managed by the GeoForschungsZentrum (GFZ), the German Research Centre for Geosciences, in Potsdam, Germany. CHAMP was equipped with the STAR (Spatial Triaxial Accelerometer for Research) accelerometer, whose acceleration precision was  $3.0 \times 10^{-9}$  m/s<sup>2</sup> within 0.1 Hz (Bruinsma et al., 2004).

The GRACE constellation consisted of a pair of satellites (GRACE-A flying  $\sim 220$  km ahead of GRACE-B) that were launched on 17 March 2002 at an altitude of near 500 km with orbit inclination  $89.5^\circ$ . The spacecraft reentered on 10 March 2018 and 24 December 2017, respectively. GRACE's period was 95 minutes and it covered all local times in a time interval of 160 days. The accelerometer onboard GRACE was the Super-STAR instrument, with precision and cadence ten times larger than CHAMP's STAR accelerometer (Flury et al., 2008). The GRACE mission was operated by NASA and by the Deutsches Zentrum für Luft- und Raumfahrt e.V. (DLR), the German Aerospace Center. Given the similarities of both spacecraft observations, we use in this study only GRACE-A data,

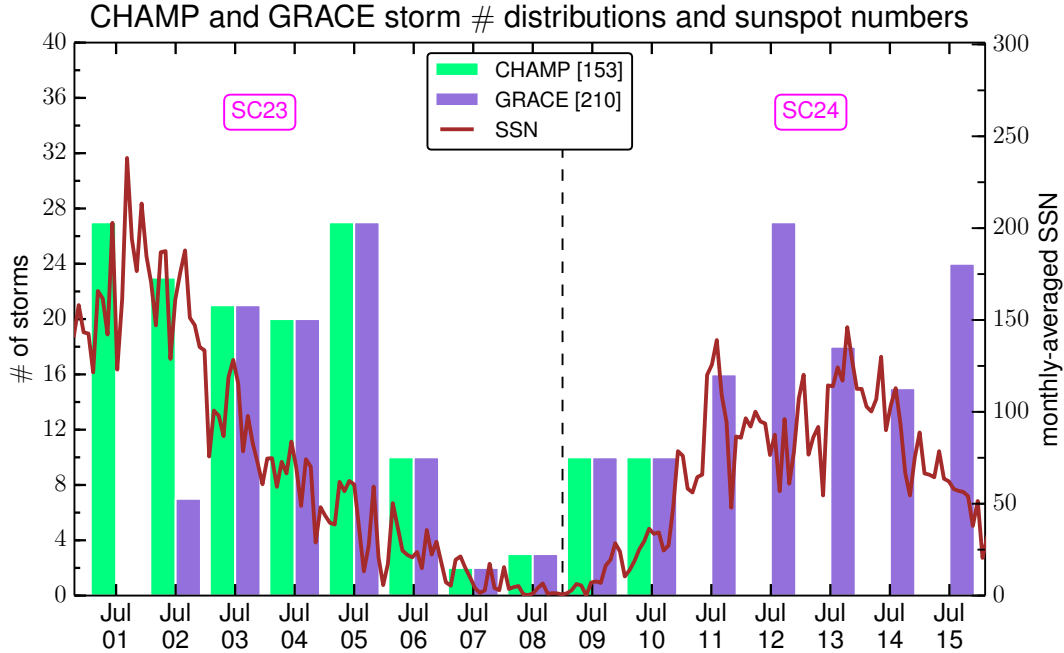


**Figure 1.** Yearly-averaged storm number distributions for CHAMP (light green bars) and GRACE (light purple bars) along with monthly-averaged SSNs (solid brown line) during the period 1 January 2001 to 31 December 2015. The vertical dashed line indicates the transition from SC23 to SC24 in January 2009. The numbers between brackets correspond to the number of events occurring during CHAMP and GRACE commission times.

henceforth GRACE data. This choice is also justified by the higher data quality presented by GRACE-A particularly after 2007.

This study is a continuation to the work of Oliveira et al. (2017), who used the whole CHAMP data available and GRACE data from the mission’s beginning up to September 2011. Now, with the addition of GRACE data from October 2011 to December 2015, it is possible to include over 50 storms in the current analysis.

The whole CHAMP data set and the first GRACE data set portion were processed by Sutton (2008). These data sets have been validated by many papers (see, e.g., Forbes, 2007; Prölss, 2011; Emmert, 2015; Zesta & Huang, 2016; He et al., 2018). The calibration method used in the latter part of the GRACE data set is described by Klinger and Mayer-Gürr (2016). A validation of the October 2011 to December 2015 GRACE data has recently been performed by Krauss et al. (2018).

## 2.4 Distribution of magnetic storm and sunspot numbers

Figure 1 represents the annual number distributions of magnetic storms occurring during CHAMP’s commission time (light green bars) and GRACE’s commission time (light purple bars) during the interval May 2001 to December 2015, according to the CME catalogue. The solid brown line indicates the SILSO monthly-averaged SSNs for January 2001 to December 2015.

Oliveira et al. (2017) presented results from the pre-maximum phase of solar cycle (SC) 23 until the beginning of SC24. SC24 began in January 2009 (dashed black line). The present work shows the additional period concerning the rising, maximum and most

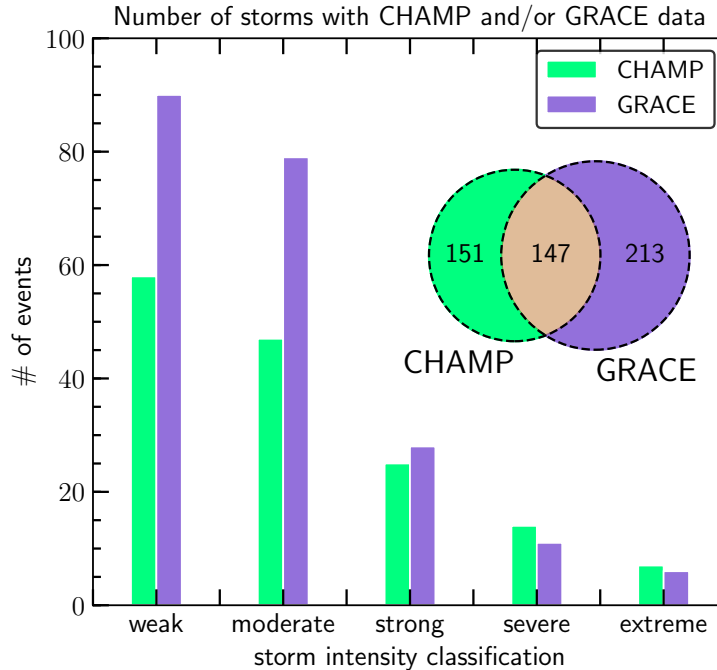


**Figure 2.** Histogram with the numbers of storms grouped by the intensity categories defined in Table 1. The Venn diagram documents the number of CHAMP and GRACE observations as well as the number of storms observed simultaneously by both missions.

of the declining phase of SC24. Therefore, the current analysis uses 15 years of neutral mass density data, a period longer than a regular SC. SC24 is noticeably weaker in comparison to SC23 as for the smaller number of SSNs observed on the Sun’s surface. The total number of storms observed by the spacecraft correlate well with SSNs, but the overall number of storms in SC24 is smaller than in SC23.

The National Oceanic and Atmospheric Administration (NOAA) provides space weather scales for magnetic storms (<https://www.swpc.noaa.gov/noaa-scales-explanation>). NOAA defines groups from 1 to 5, namely minor, moderate, strong, severe, and extreme, with respect to increasing values of the Kp index. We follow the same nomenclature as suggested by NOAA, but we define our groups in terms of the minimum value of the SYM-H index at the end of each individual storm main phase. The storm groups are summarized in Table 1. The link provided above also shows general information about the impact storms with different intensities can have on power transmission lines, satellite operations, and other technological systems.

Figure 2 shows results for the storm intensity distributions of CHAMP (light green bars) and GRACE (light purple bars), respectively. The Venn diagram in the inset plot shows that the number of storms with available data for CHAMP and GRACE are 151 and 213, respectively, whereas the total number of individual storms is 217, with 147 storms having data available from both missions. Table 1 shows the number of events with data from either CHAMP or GRACE, or both, available for each category. Zesta et al. (2018) provided a detailed description of the dynamic response of all storms, with emphasis on the extreme events shown in Figure 2.

Storm Intensity	Category <sup>a</sup>	SYM-H interval <sup>b</sup>	# of events <sup>c</sup>
Minor	G1	SYM-H $\geq -50$ nT	90
Moderate	G2	$-100 \leq$ SYM-H $< -50$ nT	78
Strong	G3	$-150 \leq$ SYM-H $< -100$ nT	28
Severe	G4	$-250 \leq$ SYM-H $< -150$ nT	14
Extreme	G5	SYM-H $< -250$ nT	7
			Total: 217 events

<sup>a</sup> Following NOAA’s nomenclature.

<sup>b</sup> This definition of storm intensity intervals is arbitrary.

<sup>c</sup> Number of events in each category with CHAMP and/or GRACE data.

**Table 1.** Definitions of Storm Intensity Categories Used in this Work.

## 2.5 CHAMP and GRACE semi-major axes

As described in section 2.3, GRACE was launched into a higher altitude ( $h$ ) in comparison to CHAMP. This reflects on the altitude variations of both satellites when flying over equatorial and polar regions. In this work, we use the semi-major axes of both satellites, measured with respect to the Earth’s center, taking into account the non-uniformity of the Earth’s radius ( $R_E$ ). Considering the Earth is flattened at the poles and bulged at the equator, and its equatorial radius  $R_{Ee} = 6,378$  km, and its polar radius  $R_{Ep} = 6,357$  km, we use a corrected expression for the Earth’s non-uniform radius as a function of  $R_{Ee}$ ,  $R_{Ep}$ , and geographic latitude ( $\theta$ ), provided by Torge (1980). In addition, we include corrections ( $a_{gp}$ ) to the semi-major axes resulting from gravitational perturbations as suggested by Chen et al. (2012). Therefore, the semi-major axes as a function of time ( $t$ ), computed in this study are given by

$$a(t) = R_E(R_{Ee}, R_{Ep}, \theta, t) + h(t) + a_{gp}(t). \quad (1)$$

The CHAMP (light green line) and GRACE (light purple line) semi-major axes are shown as a function of time in Figure 3. The thick green and purple lines show the daily-averaged  $\langle a \rangle$  semi-major axis for each mission. The sudden jumps in the CHAMP semi-major axis in 2002, 2003, 2006 and 2009 correspond to maneuver procedures used to correct the spacecraft’s altitude (Bruinsma et al., 2004). On the other hand, GRACE presented a larger semi-major axis variation and a smaller decay rate because it operated at higher altitudes. See Oliveira et al. (2017) and Krauss et al. (2018) for CHAMP’s and GRACE’s annual decay rates and altitude distributions, respectively.

## 2.6 Thermosphere empirical model

In this work, we use the Jacchia-Bowman 2008 empirical model (Bowman et al., 2008, hereafter JB2008) to compute modeled thermosphere neutral mass densities. Early versions of JB2008 used only Jacchia’s diffusion equations (Jacchia, 1970) and solar ultraviolet heating represented by the solar radio flux at wavelength 10.7 cm ( $F_{10.7}$ ) index and its average  $\langle F_{10.7} \rangle$  centered at 81-day intervals. It was noted that only taking ultraviolet (UV) heating would result in density errors with periods of approximately 27 days, or a solar rotation. Bowman et al. (2008) included semi-annual variation corrections that accounted for EUV and FUV radiations, namely extreme and far UV radiations, as well. In addition, the use of the Dst index as a replacement for the global ap index (3-hour time resolution) in the magnetic activity contribution also contributed to the improvement of the model accuracy.

The JB2008 model computes thermosphere neutral mass density from a single parameter, the local exosphere temperature, here represented by  $T_\infty$ . This temperature is



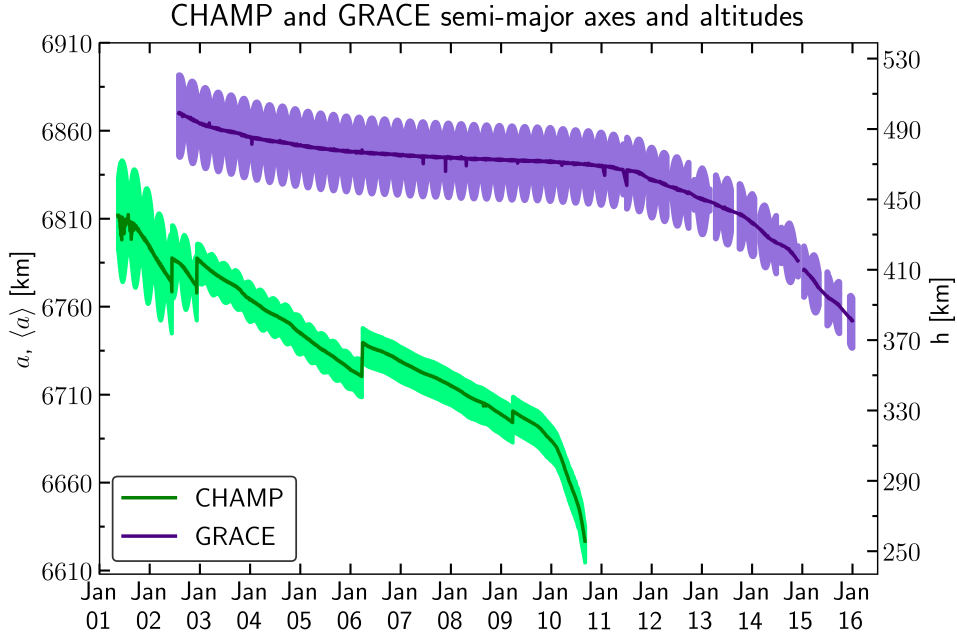


**Figure 3.** Semi-major axes  $a$ , in km, computed for CHAMP (light green line) and GRACE (light purple line) missions, with respect to the Earth’s center, according to equation 1. The dark green and purple lines indicate semi-major axis daily averages  $\langle a \rangle$  for CHAMP and GRACE, respectively. The secondary vertical axis indicates the spacecraft’s altitudes with respect to the Earth’s surface.

represented by

$$T_{\infty} = T_{\ell}(\theta, \delta_{\odot}, \tau) + \Delta T_{LST}(\tau, \theta, h) + T_{UV}(\chi) + T_{MA}(Dst), \quad (2)$$

where  $T_{\ell}$  corresponds to an empirical formula for the local exospheric temperature as a function of latitude  $\theta$ , solar declination  $\delta_{\odot}$ , and local time  $\tau$ ;  $\Delta T_{LST}$  is an altitude-dependent ( $h$ ) local solar time correction;  $T_{UV}$  is the solar contribution dependent on solar EUV and FUV irradiance as a function of solar indices  $\chi$  including X-ray and Lyman- $\alpha$  wavelengths (see review by He et al., 2018); and  $T_{MA}$  is a global correction resulting from magnetic activity and computed as a function of the Dst index according to an empirical formula provided by Burke et al. (2009).

## 2.7 Satellite orbital decay computation

Nowadays, observations of LEO satellite drag effects are performed by either ground tracking radar or accelerometers on-board the spacecraft, as for the cases of CHAMP and GRACE (section 2.3). In the case of accelerometers, the focus of this paper, the drag acceleration is given by the expression known as the drag equation

$$a_d = -\frac{1}{2}\rho C_D \frac{S}{m} V^2, \quad V = |\vec{V}_{s/c} - \vec{V}_{wind}|, \quad (3)$$

where  $S$  is the satellite area of contact with the external environment;  $C_D$  is the drag coefficient;  $m$  is the satellite’s mass;  $\rho$  is the neutral mass density; and  $V$  is the magnitude of the relative speed between the spacecraft velocity ( $\vec{V}_{s/c}$ ) and the local wind velocity ( $\vec{V}_{wind}$ ). The wind velocity corresponds to the sum of the atmospheric rotational velocity and any residual winds at the satellite’s location (Marcos et al., 2010).

From all the parameters listed in equation 3, the spacecraft's area and mass history are assumed to be well known. The drag acceleration  $a_d$  is known to be very accurate as measured by the STAR and Super-STAR instruments (see section 2.3). The relative velocity  $V$  can sometimes be a large source of errors because the residual velocities in  $\vec{V}_{wind}$  are not very well modeled and observed (Marcos et al., 2010; Prieto et al., 2014; Zesta & Huang, 2016). As a result, the drag coefficient is most of the time the major source of density errors in neutral mass density determinations according to equation 3.

The drag coefficient is a unitless macroscopic parameter that depends closely on the energy and momentum transfer between the atmospheric environment and the spacecraft. In addition,  $C_D$  depends on the geometric properties of the spacecraft, the spacecraft orientation with respect to the gas flow (angle of attack), and the physical properties of the surfaces of contact (Moe & Moe, 2005; Marcos et al., 2010; Zesta & Huang, 2016). In a review by Vallado and Finkleman (2014), the authors pointed out that for LEO satellites such as CHAMP and GRACE  $C_D$  can acquire values between 2 and 4. According to equation 3, this difference could lead to an error of 100% in the measurement of neutral densities considering only errors introduced by the drag coefficient.

Drag coefficients are usually obtained by numerical models that simulate the interaction between the atmosphere and the satellite through energy and momentum exchange (Moe & Moe, 2005; Prieto et al., 2014), and by fitting orbital drag parameters during operations (e.g., McLaughlin et al., 2011). In this study, we use the drag coefficients calculated by Sutton (2009). He employed normalized coefficients specifically for the case of satellites with elongated shapes such as CHAMP and GRACE. By using the assumption of incident molecular flow under the regime of random thermal motion with diffuse reemission, (Sentman, 1961; Moe & Moe, 2005), Sutton (2009) compared CHAMP data with High Accuracy Satellite Drag Model (HASDM) data (Storz et al., 2002) and was able to reduce the density errors by nearly 36% when these assumptions were not considered.

The satellite storm-time orbital decay rate (ODR) is calculated according to the expression (Chen et al., 2012)

$$\frac{da}{dt} = -C_D \frac{S}{m} \sqrt{GM\langle a \rangle} \Delta\rho, \quad (4)$$

where, respectively for each satellite,  $C_D$ ,  $S$  and  $m$  are the same parameters shown in equation 3. In this equation, the plate surface areas are the projected values perpendicular to the in-track direction (Doornbos, 2012; Krauss et al., 2012). Both satellites' relevant areas and mass histories are obtained from Bruinsma and Biancale (2003) and Bettadpur (2007), respectively.  $\Delta\rho = \rho - \rho_0$  is the difference between the observed and modeled background densities (see section 3).  $G = 6.674 \times 10^{-11} \text{ m}^3 \cdot \text{kg}^{-1} \cdot \text{s}^{-2}$  is the gravitational constant, and  $M = 5.972 \times 10^{24} \text{ kg}$  is the Earth's mass.  $\langle a \rangle$  is the daily-averaged semi-major axis computed by equation 1 and shown in Figure 3 for the particular time of observation.

Since the background density effects have been removed, the storm-time orbital decay (SOD) is then computed by integrating ODR over time along the satellite's path as

$$d(t) = \int_{t_1}^{t_2} a(t) dt, \quad (5)$$

where  $t_1$  and  $t_2$  are arbitrary times taken around some specific CME forcing event (CME impact time or onset of a magnetic storm main phase).

In the next section we use the 24 August 2005 magnetic storm event to illustrate our methodology. Later on, we show results of superposed epoch analyses for CHAMP

and GRACE to investigate satellite orbital drag effects and discuss the performance of the JB2008 model in predicting satellite orbital drag during our CME-driven storms.

### 3 Methodology

#### 3.1 The 24 August 2005 magnetic storm as an example

Figure 4 documents results for the 24 August 2005 magnetic storm. Modeled and observed densities, as well as decay rates and storm-time orbital decays are shown for CHAMP (left column), and GRACE (right column). The top row shows results of IMF  $B_z$  (Figure 4a1), and SYM-H (Figure 4a2). The horizontal axes indicate date and universal time.

The first dashed vertical line indicates the time of CME/shock impact (leading edge), whereas the second one represents the time in which IMF  $B_z$  abruptly turns southward (magnetic material). The first event is associated with the sudden impulse whose well-known signature is a sharp increase in ground magnetic measurements (Oliveira et al., 2018; Rudd et al., 2019), while the second event usually coincides with the storm main phase onset, when Dst/SYM-H measurements become highly depressed due to ring current energization (Gonzalez & Tsurutani, 1987; Gonzalez et al., 1994). Although compressions resulting from dynamic pressure enhancements can increase high-latitude neutral density measurements (Shi et al., 2017; Ozturk et al., 2018), storm time heating is responsible for larger and global effects on the thermospheric neutral mass density (e.g., Krauss et al., 2015; Oliveira et al., 2017).

Before the CME/shock impact, IMF  $B_z$  varies between  $\pm 5$  nT. During the shock impact,  $B_z$  decreases to almost  $-20$  nT. After the shock at 0613 UT,  $B_z$  increases to values larger than 40 nT. That is the moment of IMF  $B_z$  southward turning, at 0915 UT, when it abruptly turns from large positive values down to almost  $-60$  nT.  $B_z$  stays negative during the next 3 hours or so, reaching strong positive values, with a few excursions to negative values in the next 9 hours. Then,  $B_z$  returns to the similar behavior it showed before the CME arrival. At the moment of shock impact, a sudden impulse signature is evident from the SYM-H profile. Then, at the end of the storm main phase, SYM-H arrives at the minimum value of  $-178$  nT, which falls into the G4 (severe) storm category as shown in Table 1. The storm main phase lasted for only 3 hours during that storm, and the ring current took a few days to recover from that CME's driving effects.

The techniques used to obtain the modeled quiet-time density used in this work have been described by Oliveira et al. (2017) and Zesta et al. (2018), but here we provide a brief explanation. The ratio between observed and modeled background neutral density for the regime of low-magnetic activity (excluding storm and compression effects, i.e.,  $|\text{SYM-H}| < 30\text{nT}$ ) is fitted to a polynomial expansion to the 15<sup>th</sup> degree. The resulting fit function  $f(t)$  is then interpolated and multiplied by the background JB2008 density with the term  $T_{MA}$  in equation 2 set to zero to exclude magnetic activity effects. The modeled quiet-time density is then the product between  $f(t)$  and the background JB2008 density.

The modeled quiet-time density, here represented by  $\rho_0$ , is indicated by the orange lines in Figure 4b1 for CHAMP, and in Figure 4b2 for GRACE. The solid blue lines indicated in both panels represent the CHAMP and GRACE observed density data, respectively.

Before the CME arrival, the observed and the modeled densities agree remarkably well. This assures that the density ratio  $\rho/\rho_0$  and the density difference  $\Delta\rho = \rho - \rho_0$  are as much close to 1 and zero as possible, respectively. After the CME/shock arrival, due to CME forcing, particularly during the storm main phase,  $\rho/\rho_0 > 1$  and  $\Delta\rho > 0$  indicate density enhancements due to magnetic activity only. This is evident for the pe-

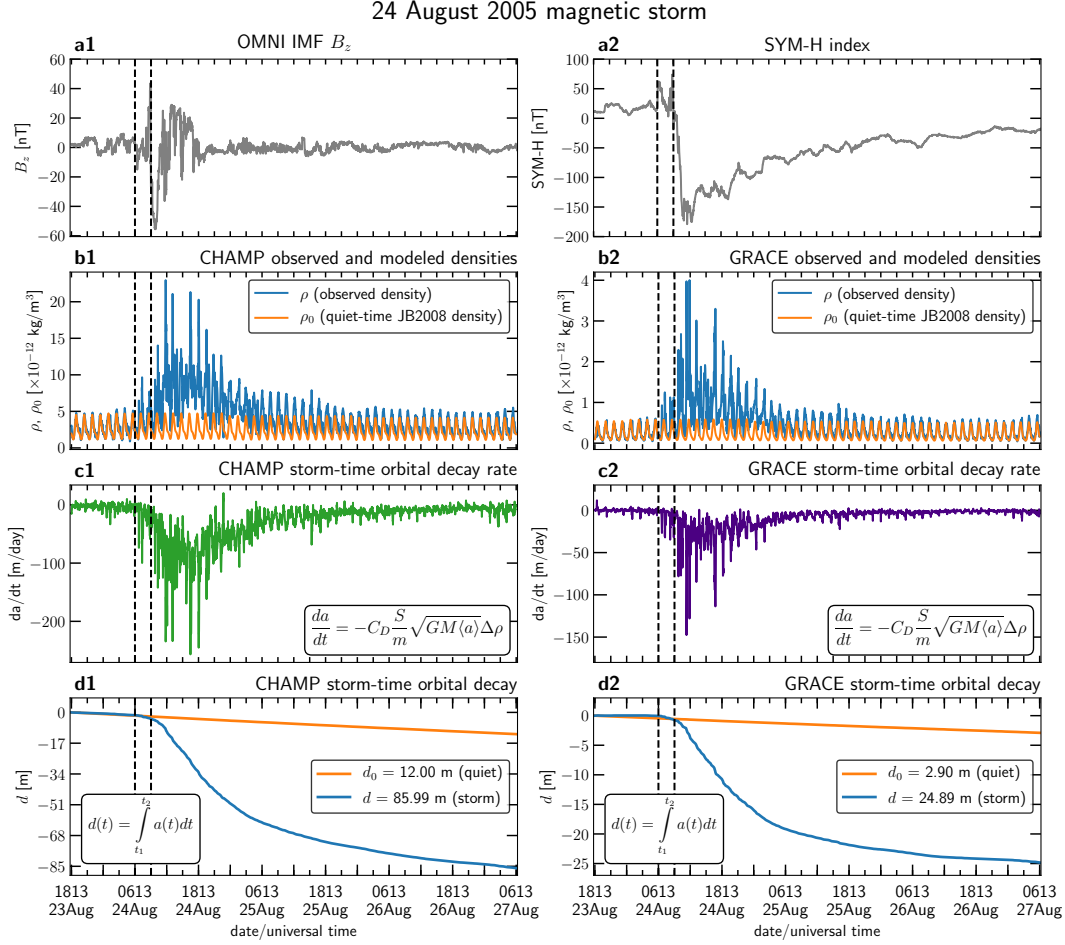


**Figure 4.** IMF  $B_z$ , SYM-H, and CHAMP/GRACE neutral mass density data for the 24 August 2005 magnetic storm. In all panels, the first dashed vertical line corresponds to the CME-shock impact, whereas the second dashed vertical line indicates the storm main phase onset. (a1), IMF  $B_z$  component; (a2), SYM-H index, both in nT. (b1-d1) and (b2-d2) indicate observed densities and quiet-time JB2008 densities, storm-time orbital decay rates ( $da/dt$ , equation 4), in m/day, and storm-time orbital decay ( $d$ , equation 5), in m, for both CHAMP and GRACE, respectively.

roids between 0613 UT and 0915 UT, due to high-latitude compression effects, and after 0915 UT, due to storm effects, as seen in Figures 4b1 and 4b2.

This is subsequently reflected on the ODRs, which are calculated by equation 4 and shown in Figure 4c1 (CHAMP) and 4c2 (GRACE). The decay rates for both spacecraft oscillate around null values before shock impact in both cases, but they are slightly noisier in the CHAMP case.  $da/dt$  starts to enhance for CHAMP and GRACE after the CME impact, but it reaches its minimum value after the storm main phase onset, leading to  $da/dt = -250$  m/day and  $da/dt = -150$  m/day for both spacecraft, respectively. The decay rate is more intense in the CHAMP case because GRACE was at higher altitudes during that storm (averaged 364.22 km and 481.95 km, respectively), leading to larger  $\Delta\rho$  in the CHAMP case. Particularly for that storm, large  $da/dt$  values for CHAMP were typically two times larger than GRACE  $da/dt$  values.

The SOD, as calculated by equation 5, is shown for CHAMP (Figure 4d1) and GRACE (Figure 4d2). In both panels, the solid orange lines indicate the orbital decays ( $d_0$ ) of both satellites if there was no storm occurring, with  $d_0 = 12.00$  m for CHAMP, and  $d_0 = 2.90$  m for GRACE, at the end of the 72-hour storm interval. In contrast, the solid blue lines show the actual storm contribution to the orbital decay. Before CME arrival,  $d(t)$  is close to zero for both spacecraft. It slightly decreases after the CME impact/compression, but it decreases abruptly after storm main phase onset. CHAMP's total decay is  $\sim -86$  m, while GRACE's decay is almost 3.5 times weaker,  $-25$  m. This example clearly shows that storms can produce significant orbital drag effects on LEO satellites, which could be nearly 10 times larger than the drag effects during low or quiet magnetic conditions. Our drag effect results agree remarkably well with the results of Krauss et al. (2018) for the very same magnetic storm within similar time intervals.

### 3.2 Modeled/observed data comparison for the 20 November 2003 magnetic storm

In this subsection, we use the 20 November 2003 magnetic storm to investigate the JB2008 model performance in computing neutral mass density and predicting orbital drag effects. This storm had  $-492$  nT as the minimum SYM-H value, and is hitherto the most extreme magnetic storm in the era of high-precision accelerometers on-board LEO satellites.

The results are shown in Figure 5, displayed in the same fashion as in Figure 4, but with two differences. First, data (left column) and model (right column) results are shown for GRACE only; second, the modeled storm-time density data is computed by using the full magnetic activity contribution to the exospheric temperature provided by the JB2008 model, meaning the term  $T_{MA}$  is not zero in equation 2.

The general IMF  $B_z$  and SYM-H index dynamics are very similar to the 24 August 2005 magnetic storm. Minimum  $B_z$  (Figure 5a1) reached almost  $-60$  nT in both storms, but it stayed southward-oriented for nearly 12 hours in the 2003 storm. This reflects on the duration of the main phase of the 2003 storm since it lasted longer and the minimum SYM-H value was much lower than in the case of the 2005 storm (Figure 5a2); however, the ring current during the 20 November 2003 storm recovered faster in comparison to the 24 August 2005 magnetic storm. This result is consistent with the works of Aguado et al. (2010) and Cid et al. (2013), who performed modeling and experimental studies to conclude that, in general, the more intense storms are associated with faster magnetospheric recovery times.

Figure 5b1 shows the same trends as seen for the observed cases for CHAMP and GRACE in Figure 4b1 and 4b2. However, the modeled density shown in Figure 5b2 shows a slightly different behavior. In spite of the fact that JB2008 captured the density dynamics remarkably well, it overestimated densities during quiet times, underestimated densities during storm times, particularly the largest values, and overestimated densities again during storm recovery phase. The density overestimation of the pre-storm data may be due to carbon dioxide ( $\text{CO}_2$ ) cooling effects during quiet times (Mlynczak et al., 2014). On the other hand, the density underestimation during storm times may be due to the inability of the model to capture the spikes, but corrections to the exospheric temperature estimation may alleviate this deficiency (Sutton, 2018). Finally, the density overestimation during storm recovery phase may be a result of the super-production of nitric oxide (NO), that has a high cooling power effect on the thermosphere through infrared emissions (Kockarts, 1980; Mlynczak et al., 2003; Knipp et al., 2017). These effects are also seen in the observed and modeled decay rates (Figures 5c1 and 5c2), where the most enhanced values of  $da/dt$  computed by the JB2008 model can be 100% smaller than the observed  $da/dt$  values.

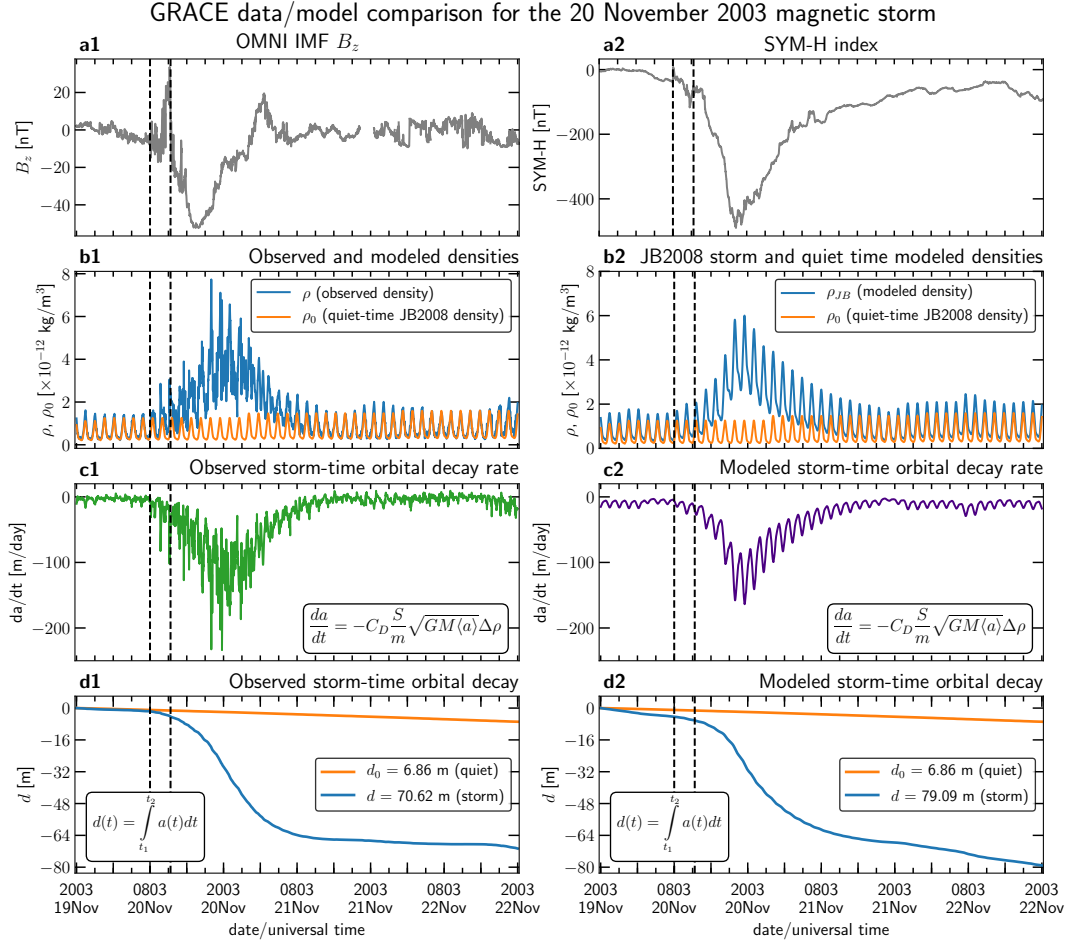


**Figure 5.** The same as in Figure 4, but for GRACE observed data (left column) and GRACE modeled data (right column) for the 20 November 2003 magnetic storm. This is not only the most extreme storm of SC23, but also the most extreme storm of the era of high-accuracy satellite data provided by the CHAMP and GRACE missions.

The SOD for GRACE during the 20 November 2003 storm was  $-70.62$  m during the 60-hour storm interval shown in Figure 5d1. This SOD also agrees well with the results of Krauss et al. (2015) for the same event. This is more than 10 times larger than the orbital decay considering the same conditions during quiet times ( $d_0 = -6.85$  m). In contrast, as shown in Figure 5d2, the modeled SOD is  $-79.09$  m, which shows a moderate overall agreement with the observations, with relative error of  $\sim 12\%$ . This is the result of the error superposition produced by the overestimation and underestimation intervals discussed above. This result shows that our method applied to long-term modeled orbital decay computations produces good results for predicting LEO satellite orbital decay during the most extreme magnetic storm in our data set, but it is not appropriate to reproduce the storm hour-by-hour dynamics correctly. This suggests the model needs to be updated in order to predict and forecast satellite orbital decay in short-time intervals with more precision.

## 4 Statistical results

In this paper, we use the technique of SEA to investigate statistical patterns and dynamics of ODRs and SODs during magnetic storms with different intensities. The SEA technique is used when a quantity is highly dynamic in a variable system. Apparently this technique was introduced in our community by Chree (1913), who superposed SSN frequency and the daily range of magnetic declination observed at the Kew Observatory. Here, we superpose satellite orbital drag effect variations by lining up the density data with respect to the storm main phase onset for each storm. This choice of zero epoch time (ZET) coincides with the IMF  $B_z$  southward turning similar to those seen in Figures 4 and 5.

However, as pointed out by a reviewer, mixing together events where a satellite's orbit varies significantly from event to event can cause unintended weighting; storms occurring when the satellites are at lower altitudes (later in the satellite mission) are overemphasized while those occurring when the satellite is at higher altitudes (earlier in the satellite mission) are underemphasized in the average. Although this may be a caveat, we will proceed with the analysis given the limited number of events with high-quality density data, particularly the ones occurring during the most extreme magnetic storms.

### 4.1 Superposed epoch analysis - storm-time orbital decay rate (ODR)

#### 4.1.1 CHAMP storm-time ODR results

Figure 6 shows results for the storm-time ODRs associated with the CHAMP satellite. The left column indicates results for the observed  $da/dt$  (as discussed for the 24 August 2005 magnetic storm), and the middle column represents results for the modeled  $da/dt$  (as discussed for the 20 November 2003 magnetic storm). The right column shows the difference  $\Delta X = X_{mod} - X_{obs}$ , with  $X = da/dt$ , between the modeled and observed ODRs. This means that if  $\Delta X > / < 0$ , the model underestimates/overestimates ODR, respectively. The first row shows SEA results for all storms, whereas the subsequent rows show results for the storm categories with increasing intensities (Table 1). All panels in Figure 6 are centered at 12 hours and 72 hours around ZET, marked by the dashed vertical lines. The vertical axes indicate magnetic latitude (MLAT), in degrees. MLAT data are allocated in 5-degree bins, whereas epoch time data are allocated in 15-minute bins.

For all storms, observed  $da/dt$  in Figure 6a1 shows similar patterns as reported by Oliveira et al. (2017) for latitudinal thermosphere heating: observed  $da/dt$  is first enhanced at high latitudes and later enhanced at equatorial latitudes within approximately 3 hours. This is a result of heating propagation from auroral regions towards very low latitude regions due to global wind surges and TADs (Fuller-Rowell et al., 1994; Bruinsma & Forbes, 2007; Sutton et al., 2009; Oliveira et al., 2017).  $da/dt$  enhancements are slightly stronger in the Northern Hemisphere (NH) because of altitudinal effects introduced by the inclined orbit of CHAMP. ODRs remain moderate ( $\sim -30$  m/day) until 18 hours after ZET, when the thermosphere cools first in the Southern Hemisphere (SH). As shown in Figure 6a2, the model fails to reproduce the latitudinal patterns of the  $da/dt$  enhancements seen in the previous description and reported by Oliveira et al. (2017). As a result, JB2008 underestimates  $\Delta X$  by approximately  $-12$  m/day during  $0 < t < 3$  hours, particularly at high latitudes, and later overestimates  $\Delta X$  by the same amount, with some weak underestimation around  $t = 24$  hour and  $t = 42$  hours (Figure 6a3).

The satellite drag effects for the minor storms (G1) are very weak, as seen for the observed (Figure 6b1) and modeled (Figure 6b2) ODRs. Figure 6b3 shows that JB2008 overestimates  $da/dt$  ( $\Delta X$  around 6 m/day) for the G1 storms, with exception for an underestimation interval ( $\Delta X$  around  $-6$  m/day) between  $t = 6$  hours and  $t = 12$  hours. Figure 6c1 shows that the moderate observed  $da/dt$  resembles the  $da/dt$  behavior for all storms until approximately  $t = 18$  hours, but it remains enhanced for more 18 hours mainly

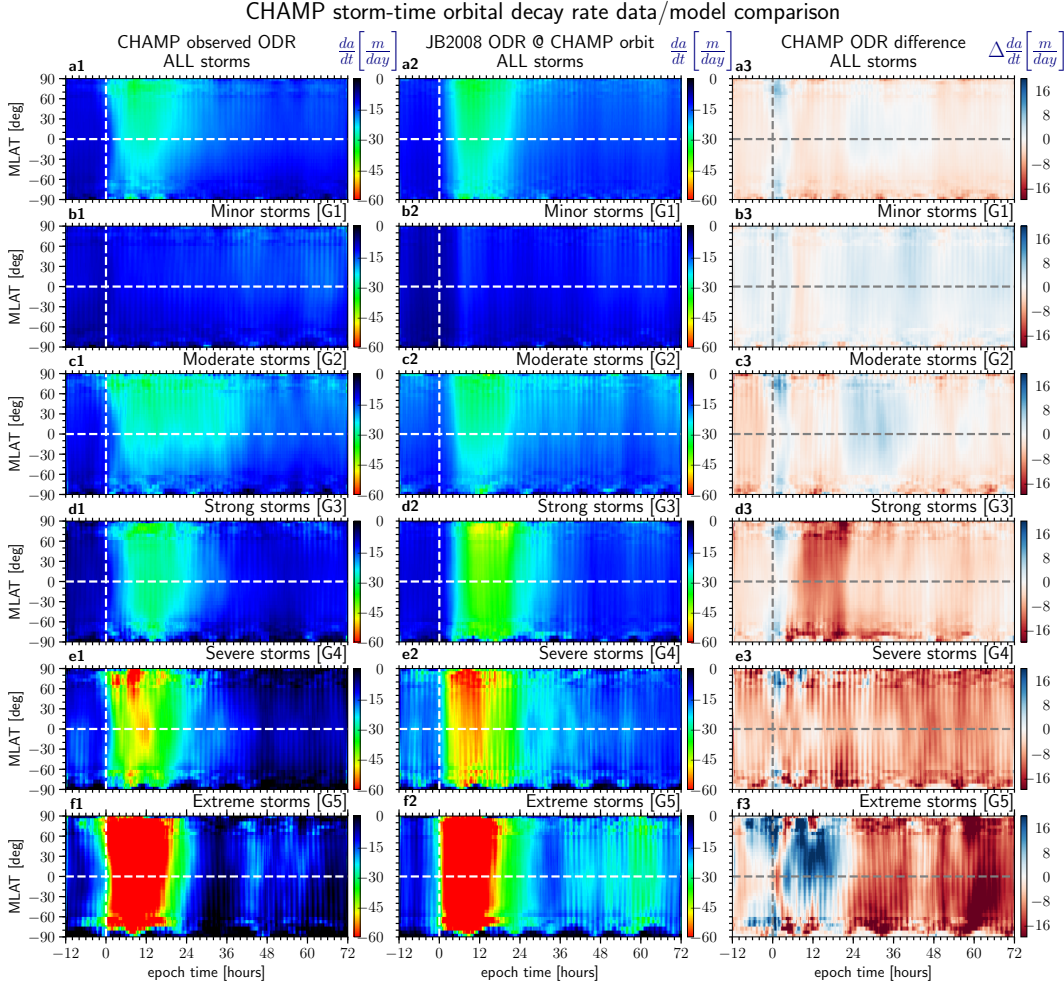


**Figure 6.** Results of superposed epoch analysis of CHAMP storm-time orbital decay rate  $da/dt$ , in m/day, calculated according to equation 4. Left column, observed  $da/dt$ ; middle column, JB2008  $da/dt$ ; and right column, difference  $\Delta X = X_{mod} - X_{obs}$ , with  $X = da/dt$ . First row indicates results for all events, while the second to the sixth rows indicate results for storms with increasing intensities (Table 1). The latitudinal data are binned in 5-degree bins, whereas the epoch time data are binned in 0.25-hour bins.

in the NH. The model results look similar, but the latitudinal heating distribution does not appear in the model results (Figure 6c2). There is some overestimation within 3 hours after ZET for the G2 storms (Figure 6c3), but the overall model performance is of overestimation, with some worse points at both hemispheres' high latitudes, particularly in the SH. However, orbital decay rates tend to persist longer in this category. For the case of strong storms (G3, Figure 6d1), the observed ODR is strong between  $0 < t < 22$  hours, particularly in the NH. The modeled  $da/dt$  levels stay strong until  $t = 26$  hours, but are stronger than the observed results particularly in the NH (Figure 6d2). The model does not reproduce latitudinal heating propagation due to TADs, and the model overestimates ODR during  $6 < t < 22$  hours, and later particularly for the SH high latitudes (Figure 6d3). Observed and modeled  $da/dt$  results for the severe storms (G4) are similar to the G3 storm results, but are clearly more intense, particularly in the NH (Figures 6e1 and 6e2). Clearly G4 storm orbital drag effects are overestimated by JB2008, and  $\Delta X < -$



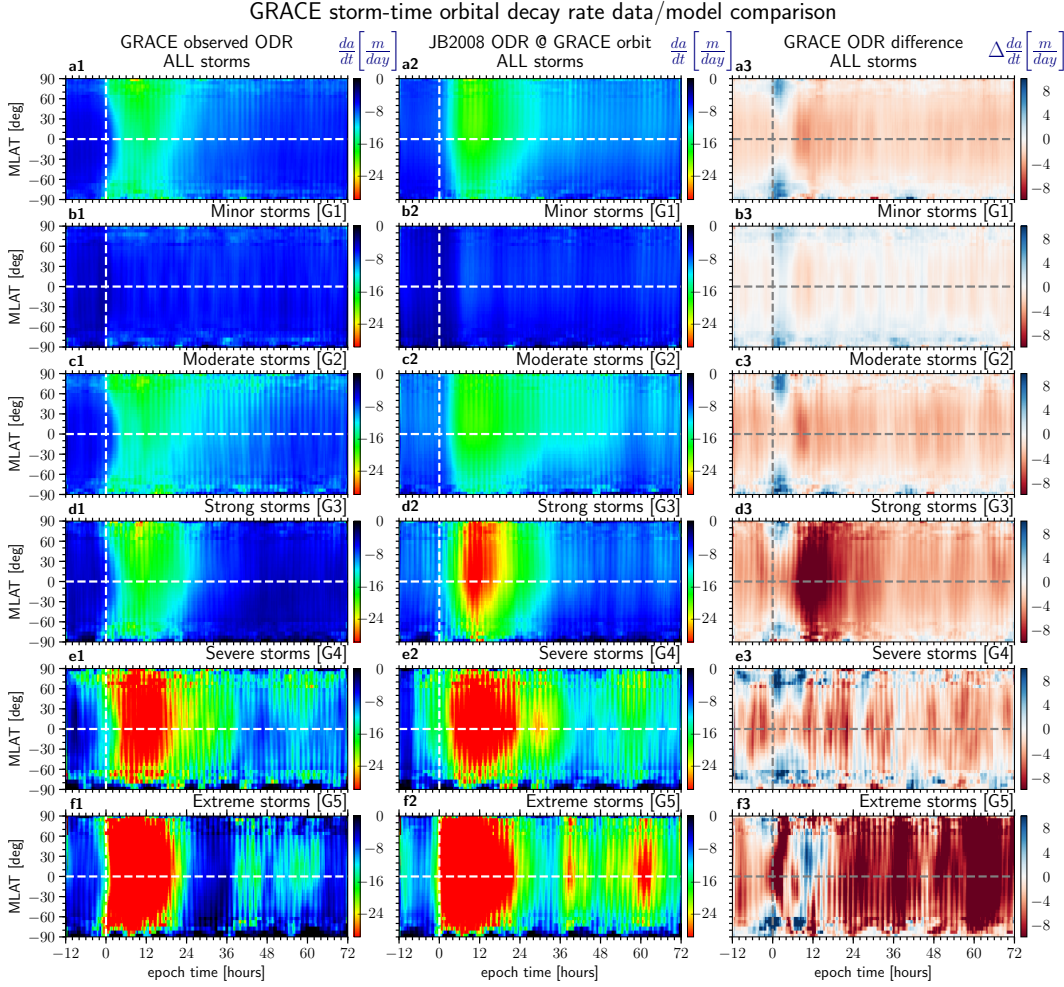
10 m/day in all latitudes with  $\Delta X < -16$  m/day appearing every other 6 hours (Figure 6e3).

The results shown for the G5 (extreme) storms in the last row of Figure 6 indicate a significantly distinct behavior in comparison to all storms in the other groups, or for all storms combined. Some observed  $da/dt$  enhancements are seen at high and middle latitudes before ZET (Figure 6f1) due to the CME/shock impacts preceding the onset of the storm main phases (Oliveira et al., 2017; Shi et al., 2017; Ozturk et al., 2018). In addition, right at  $t = 0$ , ODRs are strongly enhanced at high- and mid- latitude to values much more intense than those shown in the other storm intensity categories, with  $da/dt < -60$  m/day.  $da/dt$  becomes intensely enhanced at equatorial latitudes due to TAD propagation, which occurs in less than 1.5 hour, half the average time of 3.0 hours found by Oliveira et al. (2017) for all storms. As for the modeled  $da/dt$ , Figure 6f2, the model satisfactorily reproduces the observed  $da/dt$  behavior until  $t = 18$  hours (except the TAD propagation after ZET), but the model overestimates orbital drag effects throughout the storm recovery phase. Perhaps the model, due to its statistical and empirical nature, did not capture the overall heating by TAD propagation as seen in the observation case because the model uses the Dst index, with time resolution of 1 hour, for the magnetic activity contribution (equation 2).

Yet for the extreme events, observations show a first cooling of the thermosphere at around  $t = 18$  hours in the SH and 3 hours later in the NH, where  $da/dt$  increases from less than  $-60$  m/day to  $-40$  m/day. At  $t = 24$  hours, a secondary cooling occurs in both hemispheres, and slightly later at middle and low latitudes in the NH, leading the thermosphere to  $da/dt$  levels similar to pre-storm levels. This is probably due to enhancements of NO at CHAMP's altitude, leading to a very fast and effective thermostat effect resulting from the competition between the storm time heating and the NO cooling (Mlynczak et al., 2003; Knipp et al., 2017; Zesta et al., 2018). However, this sudden cooling is not evident in the JB2008 results. The model in fact overestimates  $da/dt$  particularly after  $t = 23$  hours, but the cooling occurs more symmetrically in all latitudes. The comparison between observation and model results (Figure 6f3) shows that the model underestimates ODR during  $0 < t < 12$  hours, slightly underestimating  $da/dt$  at middle and low latitudes and some overestimation at high latitudes. However, the model significantly overestimates ODRs ( $\Delta X < -18$  m/day) at high latitudes around  $t = 20$  hours and almost at all latitudes at  $t > 24$  hours. This clearly shows that the model cannot capture NO cooling effects during the recovery phases of extreme storms at this time (Bowman et al., 2008; Knipp et al., 2013, 2017; Zesta et al., 2018), although early efforts have been undertaken in order to capture JB2008 averaged cooling effects for CHAMP and GRACE for larger time spans (Weimer et al., 2011).

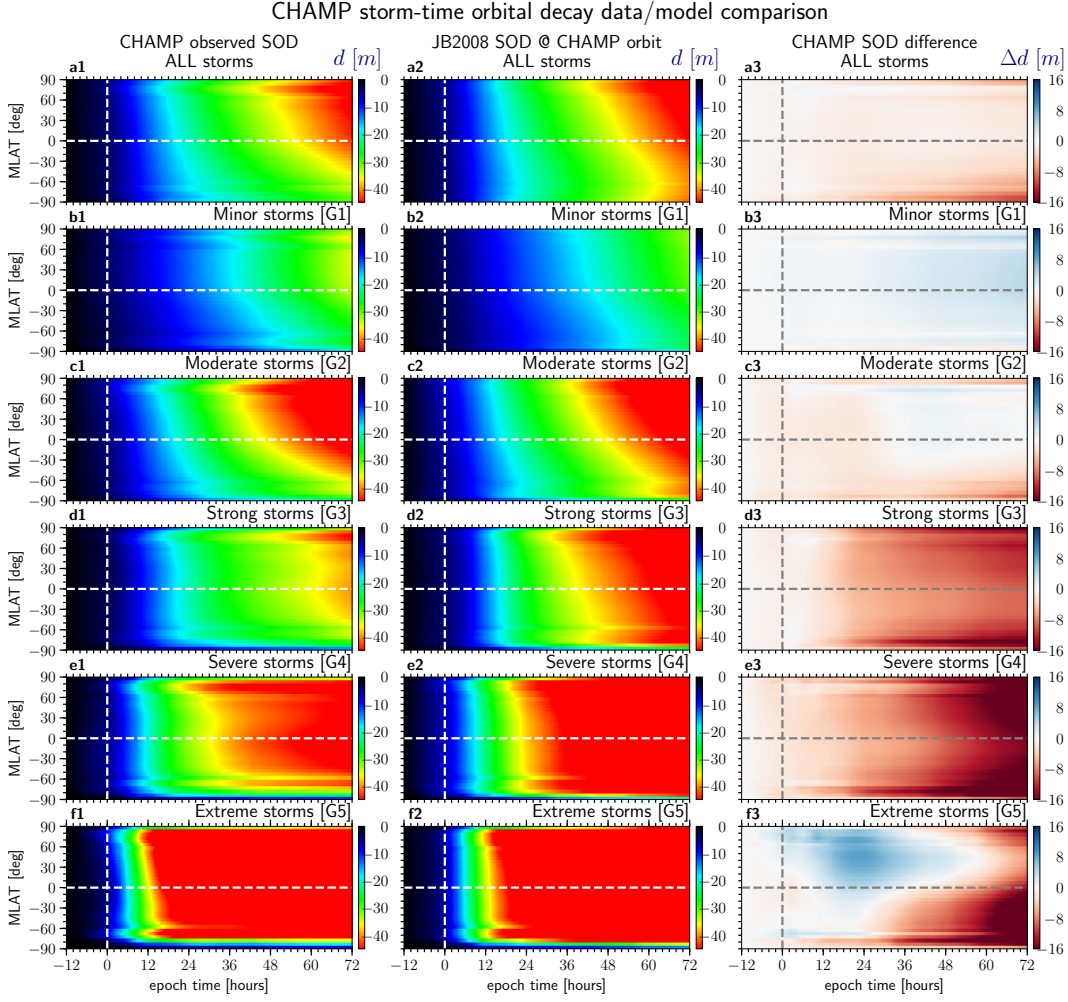
#### 4.1.2 GRACE storm-time ODR results

Figure 7 shows ODR results for GRACE plotted in the same way as in Figure 6. One of the main differences corresponds to the smaller  $da/dt$  levels (around half) in comparison to CHAMP, because GRACE was always at higher altitudes than CHAMP. This confirms results by Chen et al. (2012) and Krauss et al. (2018). In this case the general JB2008 model performance for all storms is worse than the model performance in the CHAMP case (Figures 7a1-a3). JB2008 overestimates orbital drag effects at almost all latitudes, being worse at mid and low latitudes. Even for the minor storms the model performance is worse (Figure 7b3). Figure 7c1 shows that the NH  $da/dt$  of GRACE G2 storms persist longer in the NH in comparison to storms in the other categories. Similarly to CHAMP's strong storms (group G3),  $da/dt$  during storms in the same group in the case of GRACE are highly (although strongly) overestimated at low and equatorial latitudes after ZET during  $6 < t < 18$  hours. For the severe storms (G4), the model overestimates ODRs in low/middle high latitudes and underestimates ODRs in high latitudes (Figures 7e1-e3).



**Figure 7.** Superposition of GRACE storm-time orbital decay rate  $da/dt$  performed in the same fashion as in Figure 6.

In all cases for GRACE so far,  $da/dt$  latitudinal heating caused by TAD propagation is poorly reproduced by the model. That is the same for the extreme (G5) storms. The data show rapid and intense heating propagation from auroral to equatorial zones in a similar way as for the CHAMP case, but the thermosphere cooling effects ( $t = 18$  hours) are slightly different. As shown in Figure 7f1, the observed  $da/dt$  decreases first at high latitudes being followed by mid and low latitudes within 1.5 hour. The observed results look very similar to the JB2008 results at that time. However, ODRs are overestimated between 36 hours and 46 hours and again between 48 hours and 66 hours, with highly overestimated  $da/dt$  levels at  $t = 62$  hours at low latitudes. As a result, as seen in Figure 7f3, the  $da/dt$  difference for the G5 storms are very high after  $t = 20$  hours for all latitude regions, in addition to high overestimation during  $0 < t < 3$  hours at high latitudes particularly in the NH. Again, the  $da/dt$  overestimation during the recovery phases of the extreme storms observed by GRACE result from the lack of NO cooling effects computed by the model (Knipp et al., 2013, 2017).



**Figure 8.** Results of CHAMP superposed epoch analysis for the storm-time orbital decay  $d(t)$  (equation 5), in m. All panels correspond to similar analyses as in Figure 6. Since the time resolution of the data is the size of each bin, or 15 minutes,  $d(t)$  in each latitudinal bin corresponds to the temporal cumulative sum along each latitude bin.

## 4.2 Superposed epoch analysis - storm-time orbital decay (SOD)

### 4.2.1 CHAMP SOD results

SODs as calculated from equation 5 are shown for the CHAMP SEA in Figure 8. The general format, time range, and data binning are the same as in Figure 6. Since the time intervals are the same for all latitude bins,  $d$  is the cumulative sum of  $da/dt$  along all latitude bins over time. That is the reason why SODs decrease in all latitude regions as time progresses.

For all storms (first row), observations show that significant orbital decay ( $d < -30$  m) occurs first at high latitudes in the NH around  $t = 14$  hours and then gradually intensifies towards SH high latitudes in the next 6 hours or so (Figure 8a1). This results from the general high NH levels shown by  $da/dt$  in Figure 6a1 which lead to high  $d$  values at high latitudes. As shown in Figure 8a2, the model performs relatively well for all storms, with low difference  $\Delta d$  levels ( $\sim -6$  m) in SH high latitudes during recovery phase (Figure 8a3). Figures 8b1-b3 show that, in general, the same occurs for the minor (G1)

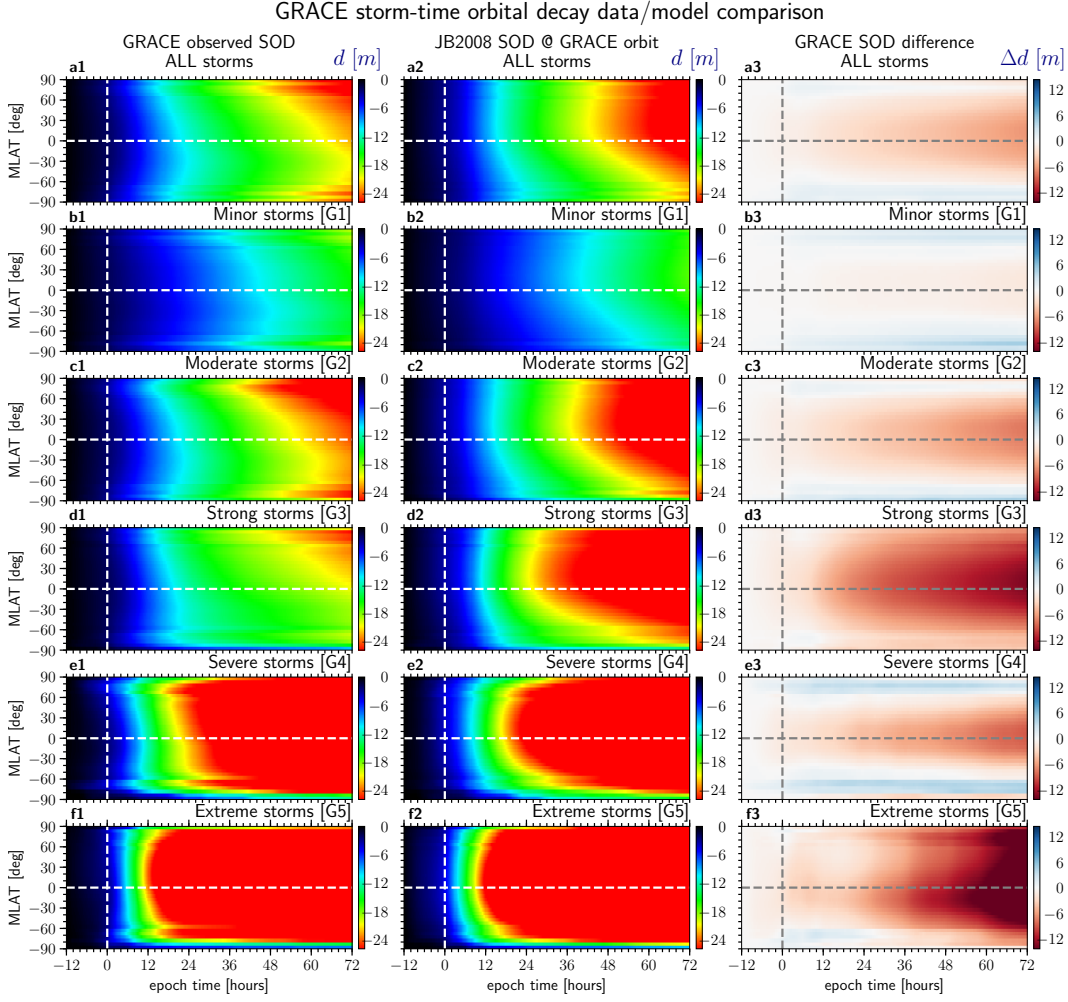


**Figure 9.** Superposition of GRACE storm-time orbital decay  $d(t)$  performed in the same fashion as in Figure 8, and calculated from data plotted in Figure 7.

storms, but total decay levels are smaller and occur later. However, the model mostly underestimates SODs during storm and recovery times. The overall behavior of storms in the moderate (G2, Figure 8c1) category resembles the general behavior of all storms, with  $d$  being more intense later during storm recovery phase, particularly at the NH high latitudes. The model  $\Delta d$  performance is very similar to the model  $\Delta d$  for all storms (Figure 8a3). In the case of strong (G3) storms, the model overestimates SODs particularly at the NH high latitudes. As seen in Figure 8e1, the severe (G4) storms are highly overestimated by JB2008. Data observations show that  $d$  reaches  $-30$  m around  $t = 12$  hours, and  $d$  near  $-40$  m is reached around  $t = 18$  hours at a small high-latitude range in the NH and at other latitudes around 26 hours. In contrast, the model overestimates  $d$  for these storms, where they reach values smaller than  $-60$  m around  $t = 12$  hours first at NH high latitudes and later increasingly at lower latitudes. The overall  $\Delta d$  is relatively high for severe storms observed by CHAMP. The observed moderate storm effects are more intense than the observed strong events because  $da/dt$  stayed enhanced longer in the moderate storm group as shown in Figure 6c3.

As for the extreme storms, data show that satellites decay much faster in comparison to the other storm categories or all storms combined, with the SH being led by the

NH by  $\sim 6$  hours (Figure 8f1). Observed SOD reaches  $-30$  m and values smaller than  $-40$  m around 3 hours and 12 hours after ZET, and becomes even smaller at all latitudes during storm main phase and storm recovery phase. The model reproduces the general observed  $d$  patterns quite well, except for the high-to-low TAD propagation (Figure 8f2). As a result and shown in Figure 8f3, JB2008 moderately underestimates SODs between ZET and  $t = 36$  hours, particularly for the NH, while it overestimates SOD in the SH after  $t = 30$  hours, more strongly for  $t > 60$  hours.

#### 4.2.2 GRACE SOD results

Figure 9 shows the latitudinal distribution for the SODs occurring during storms observed by GRACE. Here,  $d$  is calculated and plotted in the same way as in Figure 8. The GRACE  $d$  levels are smaller than the CHAMP  $d$  levels as a consequence of the higher GRACE altitude. For all storms, the total observed  $d$  response occurs first at high latitudes, being slightly earlier in the NH, and then their effects spread toward low and equatorial latitudes. At least in comparison to the SODs at CHAMP altitudes, the GRACE SODs are more susceptible to energy propagation effects due to TADs at GRACE altitudes. This pattern is similar for all storm categories from G1 to G4 categories, with the satellite decaying faster with increasing storm intensity. The exception is for the moderate storms (Figure 9c1), which show more intense  $d$  values in comparison to strong storms (Figure 9d1). However, the model fails to capture TAD effects in these categories because total orbital decay becomes more intense at low and middle latitudes before the high latitudes. As a result, the SOD differences are high in the low latitude regions, particularly for the moderate (G2) and strong (G3) storm categories (Figures 9c3 and 9d3).

Surprisingly, Figure 9f1 indicates that the SOD observed by GRACE during extreme storms show a different behavior in comparison to the other storm categories. This behavior is different from the behavior of the extreme storms in the case of CHAMP.  $d$  reaches  $-15$  m 6 hours after ZET at the equator and then gradually decreases toward high latitudes of both hemispheres in the following 6 hours (see discussion below). Although the model performance when reproducing SODs is remarkably good between ZET and 24 hours for the extreme storms (Figure 9f2), later  $\Delta d$ 's increase at mid- and low latitudes in the SH and at high and middle latitudes in the NH hemisphere (Figure 9f3). This is a result of density overestimation by JB2008 during recovery phases of extreme storms, possibly associated with the lack of NO cooling effects accounted for by the model, as shown in Figures 4 and 5.

The corresponding CHAMP and GRACE  $da/dt$  results for the G5 storms (Figures 6f1 and 7f1), plotted for an enlarged colorbar range, are shown with more detail in Figure 10 for CHAMP (top) and GRACE (bottom). CHAMP ODRs are enhanced first at high latitudes and propagate equatorward within 1.5 hour ( $da/dt \sim -75$  m/day), but stronger ODR enhancements ( $da/dt \sim -100$  m/day) are seen occurring during early storm main phase at equatorial latitudes around the second orbit. In the case of GRACE, this effect is more evident because strong ODR effects ( $da/dt < -60$  m/day) are observed at equatorial latitudes nearly 3 hours after ZET. As a result, this explains the strong  $d$  response for GRACE occurring first at equatorial latitudes which are observed first at the NH high latitudes for CHAMP (Figures 8f1 and 9f1, respectively). Such signatures are consistent with either the global redistribution of high-latitude Joule heating (see, e.g., Fuller-Rowell et al., 1994; A. Richmond & Lu, 2000; Oliveira et al., 2017) or possibly from the direct uplift of the thermosphere through ion/neutral interactions as postulated by Tsurutani et al. (2007) and Lakhina and Tsurutani (2017). However, as pointed by the latter authors, the last hypothesis has yet to be tested by nonlinear simulations that take into account the coupling between gravity, pressure gradients, viscosity, and advection of neutral atom flow effects, along with the heating and expansion during the uplift process.

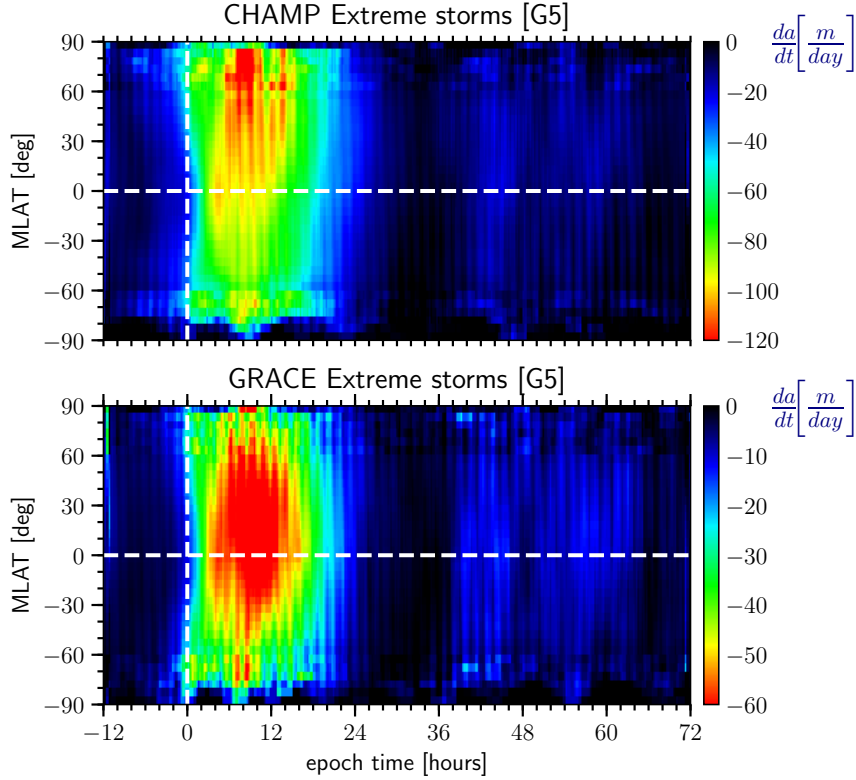


**Figure 10.** Observed CHAMP (top) and GRACE (bottom) storm-time ODRs plotted similarly to Figures 6f1 and 7f1, respectively, but with increased colorbar ranges. Strong  $da/dt$  enhancements are seen at equatorial regions for CHAMP and GRACE, but they are more intense in the case of the latter spacecraft.

### 4.3 Comparisons of modeled and observed densities

The statistical results for observed (solid blue line) and modeled (solid orange line) neutral mas densities are obtained for CHAMP (Figures 11) and GRACE (Figure 12), respectively. They are computed by averaging  $\rho$  over all latitude bins for each particular 15-min temporal bin. Then since density assumes always positive values, a Monte Carlo/Savitzky-Golay filter scheme is applied to the obtained time series in order to smooth  $\rho$  locally. This method eliminates local spikes and yields more accurate averages for each temporal bin. See details in Oliveira et al. (2017).

Figure 11a shows results for all CHAMP-observed storms, while (b-f) respectively show results for the same storms in the groups G1 to G5 as shown in Table 1. The dashed vertical lines indicate ZET, and the time range of the plots spans around 12 hours before and 72 hours after ZET. In general, both spacecraft and JB2008 densities show that peak values occur the earlier the more intense the storm category. In addition, results show that the model follows the same dynamic response as shown by the observations, with the model underestimating and overestimating densities during intervals of 3-6 hours for all storms (Figure 11a), minor storms (b) and moderate storms (c).

CHAMP results for the strong (G3) storm category, Figure 11d, show that JB2008 highly overestimated densities in the interval  $3 < t < 24$  hours, which explains the high ODR levels shown in Figure 6d3 and the large SOD difference for  $t > 24$  hours in Figure 8d3. For the severe (G4) storms, JB2008 overestimates densities for  $t > 6$  hours and

## CHAMP neutral density: observation and model comparison

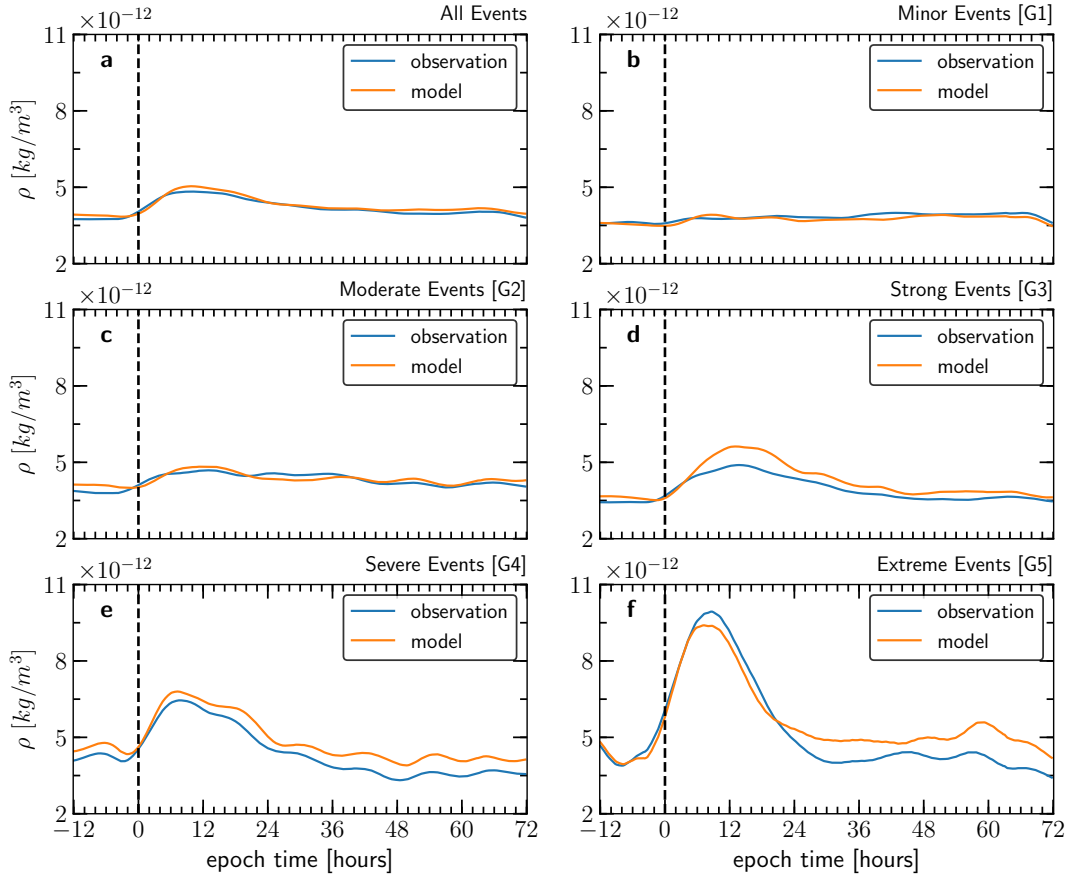


**Figure 11.** Superposition of observed CHAMP densities (solid blue lines) and for the modeled CHAMP densities (solid orange lines). (a) indicates results for all storms, while (b-f) indicate results for storms in the groups G1-G5 (Table 1). Results are shown in the time interval  $(t_1, t_2) = (-12, 72)$  hours around zero epoch time. The Monte Carlo/Savitzky-Golay smoothing scheme of Oliveira et al. (2017) was used in the computation.

the difference becomes stronger as time progresses. This is the reason why  $\Delta d$  becomes stronger during late storm recovery phase (Figure 8e3).

Extreme (G5) storm results show that the densities computed by JB2008 are smaller than the densities observed by CHAMP during the interval  $6 < t < 21$  hours, and the situation is inverted after  $t = 24$  hours. This explains the underestimated  $d$  values and the overestimated  $d$  values for the extreme storms shown in Figure 8f3.

As represented in Figure 12, similar trends are seen for GRACE. However, JB2008 density computations seem to agree with observations more in the case of GRACE with respect to the case of CHAMP. This is more evident for the case of severe storms (Figure 12e), except for the strong storms. Another difference occurs for the extreme (G5) storms, as indicated by Figure 12f where density is slightly overestimated in the interval  $0 < t < 6$  hours and then density agrees well with observations in the interval  $6 < t < 18$  hours. Then, density becomes highly overestimated for  $t > 18$  hours. This modeled density results explain the highly overestimated SOD shown in Figure 9f3.

## GRACE neutral density: observation and model comparison

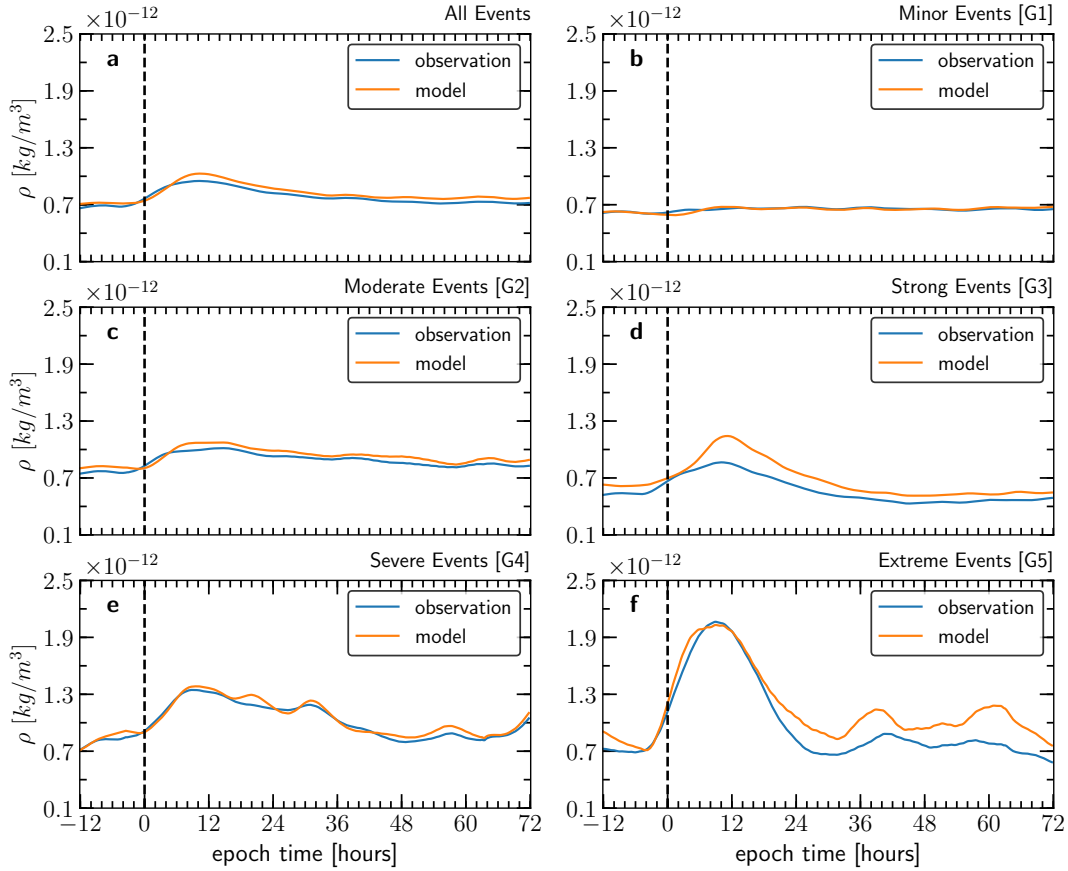


**Figure 12.** The same as for Figure 11, but for GRACE.

#### 4.4 Storm-time CHAMP and GRACE uncertainties

Now we investigate uncertainties associated with JB2008 when computing densities at CHAMP and GRACE orbits. Figure 13 shows results for the relative error  $\eta = (\rho_{mod} - \rho_{obs})/\rho_{mod}$  of the model/observation comparison calculated from the last two plots for CHAMP (Figure 11) and GRACE (Figure 12). The solid green lines indicate CHAMP results, whereas the solid purple lines indicate GRACE results. Panel (a) indicates results for all events, and panels (b-f) indicate results for storms in the categories with increasing storm intensities. The shaded light gray area corresponds to the  $\pm 5\%$  confidence interval (CI) recommended by the U.S. Air Force for acceptable orbital decay predictions, and the light orange arrows correspond to key times for the accurate knowledge of storm-time satellite orbital drag effects (Lewis, 2019).

For all storms (Figure 13a), relative errors of the CHAMP satellite behave well because they stay inside the  $\pm 5\%$  CI during storm times. The model uncertainties are higher in the GRACE case. Relative errors stay about half of the time inside the CI, being outside of it during storm main phase and late storm recovery phase. JB2008 underestimates data at CHAMP's orbit during early storm main phase and overestimates density afterwards. The same occurs for the GRACE case. Figure 13b shows that in the case of minor (G1) storms CHAMP and GRACE uncertainties were most of the time inside the CI, with JB2008 underestimating data for CHAMP's orbits. The case of moderate storms



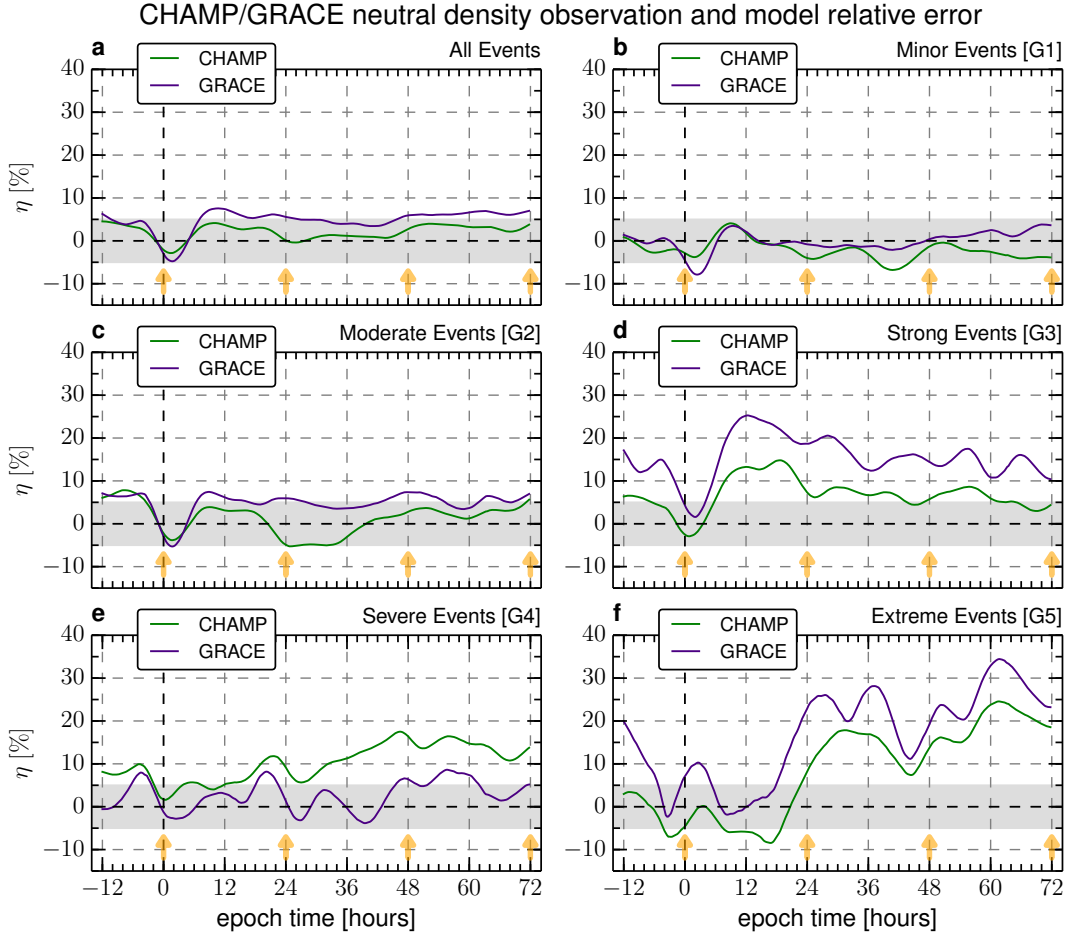


**Figure 13.** Uncertainties of densities computed by JB2008 for CHAMP (solid green lines) and GRACE (solid purple lines). Panel (a) indicates results for all storms, while panels (b-f) indicate results for the storms G1-G5 shown in Table 1.

(Figure 13c) is very similar to the case of all storms superposed, except that JB2008 underestimates density for CHAMP's orbits during the interval  $21 < t < 35$  hours.

The model behavior for the case of strong (G3) storms is quite different from the previous storm categories, as shown in Figure 13d. CHAMP and GRACE density uncertainties stay outside the CI with the GRACE uncertainties being higher than the CHAMP uncertainties. Maximum relative errors are  $\eta \sim 15\%$  for CHAMP ( $t = 18$  hours) and  $\eta \sim 25\%$  for GRACE ( $t = 12$  hours). Figure 13e shows that the situation is different in the case of the severe (G4) events, where GRACE's uncertainties are smaller than CHAMP's uncertainties. CHAMP relative errors are inside the CI during the first 12 storm-time hours, when they increase later during storm recovery phase reaching values up to 18%. GRACE uncertainties stay inside the CI most of the time, being outside of it only during the intervals  $18 < t < 22$  hours and  $44 < t < 62$  hours.

Finally, for the extreme (G5) events (Figure 13f), relative errors show that the model performance for GRACE density predictions is worse than the model performance for CHAMP density predictions. In the case of CHAMP, densities are underestimated until 22 hours after ZET when it becomes highly overestimated afterwards with relative errors as high as 25% during late storm recovery phase. In the case of GRACE,  $\eta$  is within

Storm category	CHAMP			GRACE		
	25Q	$\langle\eta\rangle$	75Q	25Q	$\langle\eta\rangle$	75Q
All Events	0.98	2.09	3.38	4.02	4.72	6.16
Minor Events [G1]	-3.69	-2.18	-1.01	-1.24	-0.15	1.23
Moderate Events [G2]	-1.49	1.22	3.25	4.11	4.81	6.40
Strong Events [G3]	4.86	6.77	8.36	12.73	15.37	18.69
Severe Events [G4]	6.22	10.15	13.88	0.02	2.69	5.47
Extreme Events [G5]	-2.11	8.30	16.97	7.84	16.60	24.97

**Table 2.** Statistical values for the CHAMP and GRACE errors, for each storm intensity category, shown in Figure 13. These values are calculated for the interval  $(t_1, t_2) = (-12, 72)$  hours. Q25 and Q75 correspond to the 25% and 75% quartiles, respectively.

the CI only during the interval  $6 < t < 18$  hours, when later it takes very high values around 35% at  $t = 62$  hours during late recovery phase.

Statistical values for the relative errors, plotted in Figure 13, for both satellites, are shown in Table 2. These values are computed over the same time spans shown in that figure. The values Q25 and Q75 correspond to the 25% and 75% quartiles of the uncertainties, respectively.

The relative errors shown in Figure 13 for both CHAMP and GRACE explain why satellite orbital drag effects are overestimated during late recovery phases of the most intense storm categories, particularly in the case of the extreme events. This effect is caused by high density values produced by JB2008, which impact the computation of orbital drag effects by increasing their uncertainties as shown by equations (4) and (5). Such overestimation effects arise because the JB2008 model does not take NO cooling effects into account when computing densities mainly during late storm main phase and subsequent storm recovery phase (Mlynczak et al., 2003; Bowman et al., 2008; Knipp et al., 2017; Zesta et al., 2018). The model should be adjusted accordingly in order to incorporate NO cooling effects into the density computation physics.

## 5 Conclusion

In this paper, we investigated the effects of atmospheric air drag forces on the orbital decays of spacecraft in low-Earth orbit during a time span longer than a regular solar cycle. We used data from two LEO satellites, CHAMP and GRACE, which flew in the upper atmosphere in two different regions separated by  $\sim 100$  km altitude, being GRACE at higher altitudes. We used a data base with 217 distinct CME-driven magnetic storms, with 151 CHAMP observations and 213 GRACE observations, totalizing 364 individual satellite observations. We computed orbital decay rates (ODRs) and storm-time orbital decays (SODs) for each satellite for all magnetic storms by using a novel method suggested by Oliveira et al. (2017) that captures density dynamics during storms. We then assessed the performance of a well-known thermosphere mass density model, namely the Jacchia-Bowman 2008 model (JB2008), by comparing observed and modeled background neutral densities, used to compute satellite orbital drag effects, by means of superposed epoch analyses with storms of different intensities. The main conclusions of this work are summarized as follows:

1. As a continuation to a previous work (Oliveira et al., 2017), we increased, with the extension of the time span from October 2011 to December 2015, our previous work by nearly 50 magnetic storms. This includes the rising, maximum, and almost all of the declining phase of SC24. We found that the overall SSNs during SC24 are smaller than SSNs in SC23. This reflects on the relative smaller num-

- ber of CMEs arriving at Earth and the subsequent number of CME-driven magnetic storms following the CME arrivals. When grouping the storms with respect to storm intensities, we found that the more intense the storm category, the fewer the number of storms in that category.
2. We found that storm-time orbital decay rates depend heavily on altitude, as suggested by previous studies (Chen et al., 2012; Krauss et al., 2018). SEA results show that CHAMP ODRs are twice larger than the GRACE ODRs.  $da/dt$  increases with storm intensity, being strongest for the extreme storm category (G5 group). Particularly for G5 storms, CHAMP and GRACE show a sudden decrease in  $da/dt$  effects probably due to high production of NO, a very efficient cooling agent in the thermosphere (Kockarts, 1980; Mlynczak et al., 2003; Knipp et al., 2017; Zesta et al., 2018). The model overestimates  $da/dt$  particularly during storm recovery phase, but for the extreme storms a slight  $da/dt$  underestimation and a strong  $da/dt$  overestimation is seen during storm main phase and storm recovery phase for both missions.
  3. The total orbital decay for CHAMP occurs first at NH high latitudes and then spread out steadily to SH high latitudes. Generally, storm-time satellite orbital drag effects increase with storm intensities, being more intense and occurring first during the strongest storms. GRACE's SOD response is very similar to CHAMP's response, but  $d$  is enhanced first at high latitudes, with the NH leading the SH by a few hours, and later storm effects become enhanced at both hemispheres' middle and low latitudes. This behavior is consistent with energy and heating distribution by global wind surge patterns and TADs (Fuller-Rowell et al., 1994; Bruinsma & Forbes, 2007; Oliveira et al., 2017). However, the extreme storms observed by GRACE show a different pattern: SOD effects at equatorial and low latitudes are more strongly enhanced with respect to the high latitudes. These effects are consistent with Joule heating propagation from high latitudes to low/equatorial latitudes (Fuller-Rowell et al., 1994; A. Richmond & Lu, 2000; Oliveira et al., 2017).
  4. When assessing performance evaluation of density predictions for each satellite orbits, we found that uncertainty levels are low for the combination of all storms and the minor (G1) and moderate (G2) storm categories. In contrast, for both satellites, we found that the storms in the strong (G3) category show high model uncertainties during late storm main phase but they decrease during storm recovery phase. For the case of severe (G4) storms, CHAMP's uncertainties are higher than GRACE's uncertainties during. CHAMP's uncertainties increase after late storm main phase and during storm recovery phase. In the case of extreme (G5) storms, uncertainties are the largest of all storm categories particularly after  $t = 20$  hours. GRACE's uncertainties are larger than CHAMP's uncertainties. We suggest that such prediction errors arise from the lack of NO cooling effects in the JB2008 model (Mlynczak et al., 2003; Bowman et al., 2008; Knipp et al., 2017; Zesta et al., 2018). Such model deficiencies should be addressed in the future for the improvement of density and satellite orbital drag predictions.

The results of this work are consistent with the results found by Bussy-Virat et al. (2018), who computed probabilities of collision between objects in space affected by thermospheric density uncertainties, as the ones introduced by magnetic storms. They found that during a severe storm (Table 1), the collision probability increased by 50%. Despite the fact that probability led to a false alarm according to their collision prediction scheme, Bussy-Virat et al. (2018) demonstrated the importance of predicting neutral densities during magnetic storms for satellite orbital drag predictions and forecasting. The results of this work point out the possible source of errors for satellite orbital drag predictions during magnetic storms, namely CO<sub>2</sub> and NO cooling effects relevant during pre-storm and recovery phase times, respectively. In addition, this is relevant to our community efforts in communicating uncertainties of space weather data and models for further improving space weather prediction and forecasting capabilities (Knipp et al., 2018).

## Acknowledgments

D.M.O. acknowledges the NASA grant HISFM18-HIF (Heliophysics Innovation Fund). E.Z. was supported by the NASA Heliophysics Internal Scientist Funding Model through the grants HISFM18-0009, HISFM18-0006 and HISFM18-HIF. The authors acknowledge the opportunities to use the CME list, SSN data, OMNI data, SYM-H data, CHAMP and GRACE data, and the JB2008 empirical model. The CME list is available at <http://www.srl.caltech.edu/ACE/ASC/DATA/level3/icmetable2.html>. The SSN data were downloaded from the website <http://www.sidc.be/silso/datafiles>. The OMNI database is located at <https://omniweb.gsfc.nasa.gov/>. The SYM-H data are available at <http://wdc.kugi.kyoto-u.ac.jp/>. CHAMP and GRACE data were obtained through access provided by the Information System and Data Center (ISDC) in Potsdam, Germany ([isdc.gfz-potsdam.de](http://isdc.gfz-potsdam.de)). The JB2008 thermosphere empirical model is available for download at <http://sol.spacenvironment.net/jb2008/>. D.M.O. also acknowledges the NSF-AGU Travel Grant for the support to attend the 2019 Chapman on Scientific Challenges Pertaining to Space Weather Forecasting Including Extremes in Pasadena, CA, where part of this work was presented.

## References

- Aguado, J., Cid, C., Saiz, E., & Cerrato, Y. (2010). Hyperbolic decay of the Dst index during the recovery phase of intense geomagnetic storms. *Journal of Geophysical Research*, *115*(A7). doi: 10.1029/2009JA014658
- Bettadpur, S. (2007). *GRACE 327-720 (CSR-GR-03-02) Gravity Recovery and Climate Experiment* (Tech. Rep. Nos. Product Specification Document (Rev 4.6 – May 29, 2012)). Austin, Texas: The University of Texas at Austin, Center for Space Research.
- Bowman, B. R., Tobiska, W. K., Marcos, F. A., Huang, C. Y., Lin, C. S., & Burke, W. J. (2008). A new empirical thermospheric density model JB2008 using new solar and geomagnetic indices. In *AIAA/AAS Astrodynamics Specialist Conference, AIAA 2008-6438*. Honolulu, HI.
- Bruinsma, S., & Biancale, R. (2003). Total Densities Derived from Accelerometer Data. *Journal of Spacecraft and Rockets*, *40*(2), 230-236. doi: 10.2514/2.3937
- Bruinsma, S., Sutton, E., Solomon, S. C., Fuller-Rowell, T., & Fedrizzi, M. (2018). Space weather modeling capabilities assessment: Neutral density for orbit determination at low earth orbit. *Space Weather*, *16*(11), 1806-1816. doi: 10.1029/2018SW002027
- Bruinsma, S. L. (2015). The DTM-2013 thermosphere model. *Journal of Space Weather and Space Climate*, *5*(A1). doi: 10.1051/swsc/2015001
- Bruinsma, S. L., & Forbes, J. M. (2007). Global observations of traveling atmospheric disturbances (TADs) in the thermosphere. *Geophysical Research Letters*, *34*(L14103). doi: 10.1029/2007GL030243
- Bruinsma, S. L., Tamagnan, D., & Biancale, R. (2004). Atmospheric densities derived from CHAMP/STAR accelerometer observations. *Planetary and Space Science*, *62*(4), 297-312. doi: 10.1016/j.pss.2003.11.004
- Burke, W. J., Lin, C. S., Hagan, M. P., Huang, C. Y., Weimer, D. R., Wise, J. O., ... Marcos, F. A. (2009). Storm time global thermosphere: A driven-dissipative thermodynamic system. *Journal of Geophysical Research*, *114*(A6). doi: 10.1029/2008JA013848
- Bussy-Virat, C. D., Ridley, A. J., & Getchius, J. W. (2018). Effects of uncertainties in the atmospheric density on the probability of collision between space objects. *Space Weather*, *16*(5), 519-537. doi: 10.1029/2017SW001705
- Chen, G.-m., Xu, J., Wang, W., Lei, J., & Burns, A. G. (2012). A comparison of the effects of CIR- and CME-induced geomagnetic activity on thermospheric densities and spacecraft orbits: Case studies. *Journal of Geophysical Research*, *117*(A8). doi: 10.1029/2012JA017782

- Chopra, K. P. (1961). Interactions of rapidly moving bodies in terrestrial atmosphere. *Reviews of Modern Physics*, *33*(2), 153–189. doi: 10.1103/RevModPhys.33.153
- Chree, C. (1913). Some phenomena of sunspots and of terrestrial magnetism at Kew observatory. *Philosophical Transactions of the Royal Society of London*, *212*(484–496), 75–116. doi: 10.1098/rsta.1913.0003
- Cid, C., Palacios, J., Saiz, E., Cerrato, Y., Aguado, J., & Guerrero, A. (2013). Modeling the recovery phase of extreme geomagnetic storms. *Journal of Geophysical Research*, *118*(7), 4352–4359. doi: 10.1002/jgra.50409
- Clette, F., & Lefèvre, L. (2016). The New Sunspot Number: Assembling All Corrections. *Solar Physics*, *291*(9–10), 2629–2651. doi: 10.1007/s11207-016-1014-y
- Doornbos, E. (2012). *Thermospheric density and wind determination from satellite dynamics*. New York, NY: Springer. doi: 10.1007/978-3-642-25129-0
- Eddy, J. A. (1976). The Maunder Minimum. *Science*, *192*(4245), 1189–1202. doi: 10.1126/science.192.4245.1189
- Emmert, J. T. (2015). Thermospheric mass density: A review. *Advances in Space Research*, *56*(5), 773–824. doi: 10.1016/j.asr.2015.05.038
- Flury, J., Bettadpur, S., & Tapley, B. D. (2008). Precise accelerometry onboard the GRACE gravity field satellite mission. *Advances in Space Research*, *42*(8), 1414–1423. doi: 10.1016/j.asr.2008.05.004
- Forbes, J. M. (2007). Dynamics of the thermosphere. *Journal of the Meteorological Society of Japan*, *85B*, 193–213. doi: 10.2151/jmsj.85B.193
- Fuller-Rowell, T. J., Codrescu, M. V., Moffett, R. J., & Quegan, S. (1994). Response of the thermosphere and ionosphere to geomagnetic storms. *Journal of Geophysical Research*, *99*(A3), 3893–3914. doi: 10.1029/93JA02015
- Gonzalez, W. D., Joselyn, J. A., Kamide, Y., Kroehl, H. W., Rostoker, G., Tsurutani, B. T., & Vasyliūnas, V. M. (1994). What is a geomagnetic storm? *Journal of Geophysical Research*, *99*(A4), 5771–5792. doi: 10.1029/93JA02867
- Gonzalez, W. D., & Tsurutani, B. T. (1987). Criteria of interplanetary parameters causing intense magnetic storms ( $\text{Dst} < -100$  nT). *Planetary and Space Science*, *35*(9), 1101–1109. doi: 10.1016/0032-0633(87)90015-8
- Gosling, J. T., McComas, D. J., Phillips, J. L., & Bame, S. J. (1991). Geomagnetic activity associated with earth passage of interplanetary shock disturbances and coronal mass ejections. *Journal of Geophysical Research*, *96*(A5), 7831–7839. doi: 10.1029/91JA00316
- He, C., Yang, Y., Carter, B., Kerr, E., Wu, S., Deleflie, F., . . . Norman, R. (2018). Review and comparison of empirical thermospheric mass density models. *Progress in Aerospace Sciences*, *103*, 31–51. doi: 10.1016/j.paerosci.2018.10.003
- Hocke, K., & Schlegel, K. (1996). A review of atmospheric gravity waves and travelling ionospheric disturbances: 1982–1995. *Annales Geophysicae*, *14*(9), 917–940. doi: 10.1007/s00585-996-0917-6
- Hunsucker, R. D. (1982). Atmospheric gravity waves generated in the high-latitude ionosphere: A review. *Reviews of Geophysics*, *20*(2). doi: 10.1029/RG020i002p00293
- Illing, R. M. E., & Hundhausen, A. J. (1985). Observation of a coronal transient from 1.2 to 6 solar radii. *Journal of Geophysical Research*, *90*(A1), 275–282. doi: 10.1029/JA090iA01p00275
- Iyemori, T. (1990). Storm-time magnetospheric currents inferred from mid-latitude geomagnetic field variations. *Journal of Geomagnetism and Geoelectricity*, *42*(11), 1249–1265. doi: 10.5636/jgg.42.1249
- Jacchia, L. G. (1959). Corpuscular radiation and the acceleration of artificial satellites. *Nature*, *183*(526), 1662–1663. doi: 10.1038/1831662a0
- Jacchia, L. G. (1970). New static models of the thermosphere and exosphere with empirical temperature profiles. In *Spec. rep. 313*. Cambridge, Massachusetts:

- Smithson, Astrophys. Obs.
- Jonas, S., & McCarron, E. D. (2016). White House Releases National Space Weather Strategy and Action Plan. *Space Weather*, *14*(2), 54-55. doi: 10.1002/2015SW001357
- Kalafatoglu Eyiguler, E. C., Kaymaz, Z., Frissell, N. A., Ruohoniemi, J. M., & Rastätter, L. (2018). Investigating upper atmospheric Joule heating using cross-combination of data for two moderate substorm cases. *Space Weather*, *16*(8), 987-1012. doi: 10.1029/2018SW001956
- Kessler, D. J., & Cour-Palais, B. G. (1978). Collision frequency of artificial satellites: The creation of a debris belt. *Journal of Geophysical Research*, *83*(A6), 2637-2646. doi: 10.1029/JA083iA06p02637
- Kilpua, E. K. J., Lugaz, N., Mays, M. L., & Temmer, M. (2019). Forecasting the structure and orientation of earthbound coronal mass ejections. *Space Weather*, *17*(4), 498-526. doi: 10.1029/2018SW001944
- King-Hele, D. (1987). *Satellite orbits in an atmosphere: Theory and applications*. Glasgow, Scotland: Blackie and Son Ltd.
- King, J. H., & Papitashvili, N. E. (2005). Solar wind spatial scales in and comparisons of hourly Wind and ACE plasma and magnetic field data. *Journal of Geophysical Research*, *110*(A2), 1-9. doi: 10.1029/2004JA010649
- Klinger, B., & Mayer-Gürr, T. (2016). The role of accelerometer data calibration within GRACE gravity field recovery: Results from ITSG-Grace2016. *Advances in Space Research*, *58*(9), 1597-1609. doi: 10.1016/j.asr.2016.08.007
- Knipp, D. J., Hapgood, M. A., & Welling, D. (2018). Communicating uncertainty and reliability in space weather data, models, and applications. *Space Weather*, *16*(10), 1453-1454. doi: 10.1029/2018SW002083
- Knipp, D. J., Kilcommons, L., Hunt, L., Mlynczak, M., Pilipenko, V., Bowman, B., ... Drake, K. (2013). Thermospheric damping response to sheath-enhanced geospace storms. *Geophysical Research Letters*, *40*(7), 1263-1267. doi: 10.1002/grl.50197
- Knipp, D. J., Pette, D. V., Kilcommons, L. M., Isaacs, T. L., Cruz, A. A., Mlynczak, M. G., ... Lin, C. Y. (2017). Thermospheric nitric oxide response to shock-led storms. *Space Weather*, *15*(2), 325-342. doi: 10.1002/2016SW001567
- Kockarts, G. (1980). Nitric oxide cooling in the terrestrial thermosphere. *Geophysical Research Letters*, *7*(2), 137-140. doi: 10.1029/GL007i002p00137
- Krauss, S., Fichtinger, B., Lammer, H., and Yu. N. Kulikov, W. H., Ribas, I., Shematovich, V. I., ... Hanslmeier, A. (2012). Solar flares as proxy for the young Sun: satellite observed thermosphere response to an X17.2 flare of Earth's upper atmosphere. *Annales Geophysicae*, *30*, 1129-1141. doi: 10.5194/angeo-30-1129-2012
- Krauss, S., Temmer, M., & Vennerstrom, S. (2018). Multiple satellite analysis of the Earth's thermosphere and interplanetary magnetic field variations due to ICME/CIR events during 2003-2015. *Journal of Geophysical Research: Space Physics*, *123*(10), 8884-8894. doi: 10.1029/2018JA025778
- Krauss, S., Temmer, M., Veronig, A., Baur, O., & Lammer, H. (2015). Thermosphere and geomagnetic response to interplanetary coronal mass ejections observed by ACE and GRACE: Statistical results. *Journal of Geophysical Research: Space Physics*, *120*(10), 8848-8860. doi: 10.1002/2015JA021702
- Lakhina, G. S., & Tsurutani, B. T. (2017). Satellite drag effects due to uplifted oxygen neutrals during super magnetic storms. *Nonlinear Processes in Geophysics*, *24*, 745-750. doi: 10.5194/npg-24-745-2017
- Lanzerotti, L. J. (2015). Space Weather Strategy and Action Plan: The National Program Is Rolled Out. *Space Weather*, *13*(12), 824-825. doi: 10.1002/2015SW001334
- Lewis, C. D. (2019). The DARPA Space Environment Exploitation (SEE) Pro-

- gram. In *2019 AGU Chapman Conference on Scientific Challenges Pertaining to Space Weather Forecasting Including Extremes*. Pasadena, CA, 11-15 February.
- Liu, H., & Lühr, H. (2005). Strong disturbance of the upper thermospheric density due to magnetic storms: CHAMP observations. *Journal of Geophysical Research*, *110*(A9), 1–9. doi: 10.1029/2004JA010908
- Lu, G., Richmond, A. D., Lühr, H., & Paxton, L. (2016). High-latitude energy input and its impact on the thermosphere. *Journal of Geophysical Research: Space Physics*, *121*(7), 7108–7124. doi: 10.1002/2015JA022294
- Lugaz, N., Farrugia, C. J., Winslow, R. M., Al-Haddad, N., Kilpua, E. K. J., & Riley, P. (2016). Factors affecting the geo-effectiveness of shocks and sheaths at 1 AU. *Journal of Geophysical Research: Space Physics*, *120*(11), 10,861–10,879. doi: 10.1002/2016JA023100
- Marcos, F. A., Delay, S. H., & Sutton, E. K. (2010). Toward next level satellite drag modelling. In *AIAA Guidance, Navigation, and Control Conference*. Toronto, Ontario Canada.
- Mayr, H. G., Harris, I., Herrero, F. A., Spencer, N. W., Varosi, F., & Pesnell, W. D. (1990). Thermospheric gravity waves: Observations and interpretation using the transfer function model (TFM). *Space Science Reviews*, *54*(3), 297–375. doi: 10.1007/BF00177800
- McLaughlin, C. A., Mance, S., & Lichtenberg, T. (2011). Drag Coefficient Estimation in Orbit Determination. *The Journal of the Astronautical Sciences*, *58*(3), 513-530. doi: 10.1007/BF03321183
- Mehta, P. M., Linares, R., & Sutton, E. K. (2018). A quasi-physical dynamic reduced order model for thermospheric mass density via hermitian space-dynamic mode decomposition. *Space Weather*, *16*(5), 569-588. doi: 10.1029/2018SW001840
- Mlynczak, M. G., Hunt, L. A., Mertens, C. J., Thomas Marshall, B., Russell III, J. M., Woods, T., ... Gordley, L. L. (2014). Influence of solar variability on the infrared radiative cooling of the thermosphere from 2002 to 2014. *Geophysical Research Letters*, *41*(7), 2508-2513. doi: 10.1002/2014GL059556
- Mlynczak, M. G., Martin-Torres, F. J., Russell, J., Beaumont, K., Jacobson, S., Kozyra, J., ... Paxton, L. (2003). The natural thermostat of nitric oxide emission at 5.3  $\mu\text{m}$  in the thermosphere observed during the solar storms of April 2002. *Geophysical Research Letters*, *30*(21). doi: 10.1029/2003GL017693
- Moe, K., & Moe, M. M. (2005). Gas-surface interactions and satellite drag coefficients. *Planetary and Space Science*, *53*(8), 793-801. doi: 10.1016/j.pss.2005.03.005
- Oliveira, D. M., Arel, D., Raeder, J., Zesta, E., Ngwira, C. M., Carter, B. A., ... Gjerloev, J. W. (2018). Geomagnetically induced currents caused by interplanetary shocks with different impact angles and speeds. *Space Weather*, *16*(6), 636-647. doi: 10.1029/2018SW001880
- Oliveira, D. M., Zesta, E., Schuck, P. W., & Sutton, E. K. (2017). Thermosphere global time response to geomagnetic storms caused by coronal mass ejections. *Journal of Geophysical Research: Space Physics*, *122*(10), 10,762-10,782. doi: 10.1002/2017JA024006
- Ozturk, D. S., Zou, S., Ridley, A. J., & Slavin, J. A. (2018). Modeling study of geospace system response to the solar wind dynamic pressure enhancement on March 17, 2015. *Journal of Geophysical Research: Space Physics*, *123*(4), 2974-2989. doi: 10.1002/2017JA025099
- Pardini, C., & Anselmo, L. (2009). Assessment of the consequences of the Fengyun-1C breakup in low Earth orbit. *Advances in Space Research*, *44*(5), 545-557. doi: 10.1016/j.asr.2009.04.014
- Picone, J. M., Hedin, A. E., Drob, D. P., & Aikin, A. C. (2002). NRLMSISE-00 empirical model of the atmosphere: Statistical comparisons and scientific is-

- sues. *Journal of Geophysical Research*, 107(A12), SIA 15-1–SIA 15-16. doi: 10.1029/2002JA009430
- Prieto, D. M., Graziano, B. P., & Roberts, P. C. E. (2014). Spacecraft drag modelling. *Progress in Aerospace Sciences*, 64, 56-65. doi: 10.1016/j.paerosci.2013.09.001
- Prölss, G. (2011). Density perturbations in the upper atmosphere caused by the dissipation of solar wind energy. *Surveys in Geophysics*, 32(2), 101–195. doi: 10.1007/s10712-010-9104-0
- Ramesh, K. B. (2010). Coronal mass ejections and sunspots – A perspective. *The Astrophysical Journal Letters*, 712(1), L77–L80. doi: 10.1088/2041-8205/712/1/L77
- Reigber, C., Lühr, H., & Schwintzer, P. (2002). CHAMP mission status. *Advances in Space Research*, 30(2), 129-134. doi: 10.1016/S0273-1177(02)00276-4
- Richardson, I. G., & Cane, H. V. (2010). Interplanetary circumstances of quasi-perpendicular interplanetary shocks in 1996-2005. *Journal of Geophysical Research*, 115(A7). doi: 10.1029/2009JA015039
- Richmond, A., & Lu, G. (2000). Upper-atmospheric effects of magnetic storms: A brief tutorial. *Journal of Atmospheric and Solar-Terrestrial Physics*, 62(12), 1115-1127. doi: 10.1016/S1364-6826(00)00094-8
- Richmond, A. D., & Matsushita, S. (1975). Thermospheric response to a magnetic substorm. *Journal of Geophysical Research*, 80(19), 2839-2850. doi: 10.1029/JA080i019p02839
- Rudd, J. T., Oliveira, D. M., Bhaskar, A., & Halford, A. J. (2019). How do interplanetary shock impact angles control the size of the geoeffective magnetosphere? *Advances in Space Research*, 63(1), 317-326. doi: 10.1016/j.asr.2018.09.013
- Sentman, L. H. (1961). *Free molecule flow theory and its application to the determination of aerodynamic forces* (Tech. Rep.). Arlington, VA: Armed Services Technical Information Agency.
- Shi, Y., Zesta, E., Connor, H. K., Su, Y.-J., Sutton, E. K., Huang, C. Y., . . . Oliveira, D. M. (2017). High-latitude thermosphere neutral density response to solar wind dynamic pressure enhancement. *Journal of Geophysical Research: Space Physics*, 122(11), 11,559-11,578. doi: 10.1002/2017JA023889
- Storz, M. F., Bowman, B. R., & Branson, J. L. (2002). High Accuracy Satellite Drag Model (HASDM). In *AIAA/AAS Astrodynamics Specialist Conference, AIAA 2002-4886*. Monterey, CA.
- Sutton, E. K. (2008). *Effects of solar disturbances on the thermosphere densities and winds from CHAMP and GRACE satellite accelerometer data* (Ph.D thesis). University of Colorado, Boulder, Colorado.
- Sutton, E. K. (2009). Normalized force coefficients for satellites with elongated shapes. *Journal of Spacecraft and Rockets*, 46(1), 112–116. doi: 10.2514/1.40940
- Sutton, E. K. (2018). A new method of physics-based data assimilation for the quiet and disturbed thermosphere. *Space Weather*, 16(6), 736-753. doi: 10.1002/2017SW001785
- Sutton, E. K., Forbes, J. M., & Knipp, D. J. (2009). Rapid response of the thermosphere to variations in Joule heating. *Journal of Geophysical Research*, 114(A4). doi: 10.1029/2008JA013667
- Tapley, B. D., Bettadpur, S., Watkins, M., & Reigber, C. (2004). The gravity recovery and climate experiment: Mission overview and early results. *Geophysical Research Letters*, 31(9). doi: 10.1029/2004GL019920
- Torge, W. (1980). *Geodesy*. Berlin, Germany: de Gruyter.
- Tsurutani, B. T., Verkhoglyadova, O. P., Mannucci, A. J., Araki, T., Sato, A., Tsuda, T., & Yumoto, K. (2007). Oxygen ion up-lift and satellite drag effects during the 30 October 2003 daytime superfountain event. *Annales Geophysici-*



- cae*, 25, 569574. doi: 10.5194/angeo-25-569-2007
- Vallado, D. A., & Finkleman, D. (2014). A critical assessment of satellite drag and atmospheric density modeling. *Acta Astronautica*, 95, 141-165. doi: 10.1016/j.actaastro.2013.10.005
- Wang, T. (2010). Analysis of Debris from the Collision of the Cosmos 2251 and the Iridium 33 Satellites. *Science & Global Security*, 18(2), 87-118. doi: 10.1080/08929882.2010.493078
- Weimer, D. R., Bowman, B. R., Sutton, E. K., & Tobiska, W. K. (2011). Predicting global average thermospheric temperature changes resulting from auroral heating. *Journal of Geophysical Research*, 116(A1). doi: 10.1029/2010JA015685
- Weng, L., Lei, J., Sutton, E., Dou, X., & Fang, H. (2017). An exospheric temperature model from CHAMP thermospheric density. *Space Weather*, 15(2), 343-351. doi: 10.1002/2016SW001577
- Yamazaki, Y., Kosch, M. J., & Sutton, E. K. (2015). A model of high-latitude thermospheric density. *Journal of Geophysical Research: Space Physics*, 120(9), 7903-7917. doi: 10.1002/2015JA021371
- Zesta, E., & Huang, C. Y. (2016). Satellite orbital drag. In G. V. Khazanov (Ed.), *Space Weather Fundamentals* (pp. 329-351). Boca Raton, FL: CRC Press.
- Zesta, E., Oliveira, D. M., Schuck, P. W., & Wilson, G. (2018). Ionosphere-thermosphere system response to extreme geomagnetic storms. In *Final paper abstract number: SM51A-08*. Presented at 2018 AGU Fall Meeting, Washington, D.C., 10-14 Dec..